THE JOURNAL OF PHYSICAL CHEMISTRY C

Feature Article

pubs.acs.org/JPCC

Panoramic View of Electrochemical Pseudocapacitor and Organic Solar Cell Research in Molecularly Engineered Energy Materials (MEEM)

Jordan C. Aguirre,[†] Amy Ferreira,[†] Hong Ding,[‡] Samson A. Jenekhe,[§] Nikos Kopidakis,[∥] Mark Asta,[‡] Laurent Pilon,[⊥] Yves Rubin,[†] Sarah H. Tolbert,[†] Benjamin J. Schwartz,*[,†] Bruce Dunn,*[,@] and Vidvuds Ozolins*[,@]

[†]Department of Chemistry and Biochemistry, University of California, Los Angeles, California 90095-1569, United States

[‡]Department of Materials Science and Engineering, University of California at Berkeley, Berkeley, California 94720-1760, United States

[§]Departments of Chemical Engineering and Chemistry, University of Washington, Seattle, Washington 98195- 1750, United States

[∥]National Renewable Energy Laboratory, Golden, Colorado 80401, United States

[⊥]Mechanical and Aerospace Engineering Department, University of California Los Angeles, 420 Westwood Plaza, Los Angeles, California 90095, United States

[@]Department of Materials Science and Engineering, University of California Los Angeles, P.O. Box 951595, Los Angeles, California 90095-1595, United States

ABSTRACT: Our program on capacitive energy storage is a comprehensive one that combines experimental and computational components to achieve a fundamental understanding of charge storage processes in redox-based materials, specifically transition metal oxides. Some of the highlights of this program are the identification of intercalation pseudocapacitance in Nb_2O_5, which enables high energy density to be achieved at high rates, and the development of a new route for synthesizing mesoporous films in which preformed nanocrystal building blocks are used in combination with polymer templating. The resulting material architectures have large surface areas and enable electrolyte access to the redox active pore walls, while the interconnected mesoporous film provides good electronic conductivity. Select first-principles density-functional theory studies of prototypical pseudocapacitor materials are reviewed, providing insight into the key physical and chemical features involved in charge transfer and ion diffusion. Rigorous multiscale physical models and numerical tools have been developed and used to reproduce electrochemical properties of carbon-based electrochemical capacitors with the ultimate objective of facilitating the optimization of electrode design. For the organic photovoltaic (OPV) program, our focus has been ongoing beyond the trial-and-error Edisonian approaches that have been responsible for the increase in power conversion efficiency of blend-cast (BC) bulk heterojunction blends of polymers and fullerenes. Our first approach has been to use molecular self-assembly to create the ideal nanometer-scale architecture using thermodynamics rather than relying on the kinetics of spontaneous phase segregation. We have created fullerenes that self-assemble into one-dimensional stacks and have shown that use of these self-assembled fullerenes lead to dramatically enhanced OPV performance relative to fullerenes that do not assemble. We also have created self-assembling conjugated polymers that form gels based on electrically continuous cross-linked micelles in solution, opening the possibility for water-processable "green" production of OPVs based on these materials. Our second approach has been to avoid kinetic control over phase separation by using a sequential processing (SqP) technique to deposit the polymer and fullerene materials in separate deposition steps. The polymer layer is deposited first, using solvents and deposition conditions that optimize the polymer crystallinity for swelling and hole mobility. The fullerene layer is then deposited in a second step from a solvent that swells the polymer but does not dissolve it, allowing the fullerene to penetrate into the polymer underlayer to the desired degree. Careful comparison of composition- and thickness-matched BC and SqP devices shows that SqP not only produces more efficient devices but also leads to devices that behave more consistently.

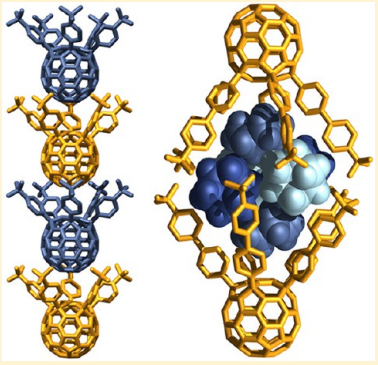

1. INTRODUCTION

Molecularly Engineered Energy Materials (MEEM) was established as an interdisciplinary DOE basic science Energy frontiers research center (EFRC) focused on fundamental studies of the mechanisms of carrier generation, transport, energy conversion, and energy storage in tunable, architectonically complex materials. The overarching objective of MEEM is to achieve transformational improvements in the performance of materials via controlling the nano- and mesoscale structure using selectively designed, earth-abundant, inexpensive molecular building blocks. MEEM includes a well-balanced combination

Received: January 29, 2014
Published: July 9, 2014

of theory, computational modeling, synthesis, characterization, and experimental measurements. From the beginning, MEEM has focused on materials that are inherently abundant, can be processed via environmentally friendly "green chemistry" routes (e.g., self-assembled from intelligently designed building blocks such as molecules and nanoparticles) and have the potential to deliver transformative economic benefits in comparison with the current crystalline- and polycrystalline-based energy technologies. Three research directions were initially identified where such novel material architectures hold great promise for high-risk high-reward research: solar energy generation using solution-processing techniques (with a focus on self-assembled architectures for organic photovoltaics), electrochemical energy storage in pseudocapacitors, and metal−organic framework materials for CO_2 capture. Of these, carbon capture was phased out in the early stages of the project to concentrate available resources on the electrochemical pseudocapacitor and organic solar cell themes. Below we give a brief review of our main achievements in these areas.

2. CAPACITIVE ENERGY STORAGE

2.1. Overview. Capacitive energy storage has been somewhat overlooked as an energy storage technology. The technology is based on electrochemical capacitors (ECs), also called supercapacitors, which store energy by either ion adsorption (electrochemical double layer capacitors or EDLCs) or fast surface redox reactions (pseudocapacitors). For traditional energy storage devices shown in Figure 1, there is a compromise between energy density and power density. Batteries and fuel cells offer high-energy density but low-power density. The "capacitors" on the low end of the energy density scale of Figure 1 refer to dielectric and electrolytic capacitors used in electronic circuits. This diagram shows that supercapacitors exist over a wide range of energy and power densities that bridge the gap between high-energy density and high-power density (i.e., between batteries and traditional capacitors). Our research project on capacitive energy storage focuses on the group of ECs known as pseudocapacitors or redox supercapacitors, which represent a class of charge storage materials that use fast and reversible surface, or near surface, redox reactions to achieve charge storage. These materials offer the prospect of maintaining the high-energy density of batteries without compromising the high power density of capacitors. It is this class of materials which offers extraordinary opportunities for capacitive energy storage.

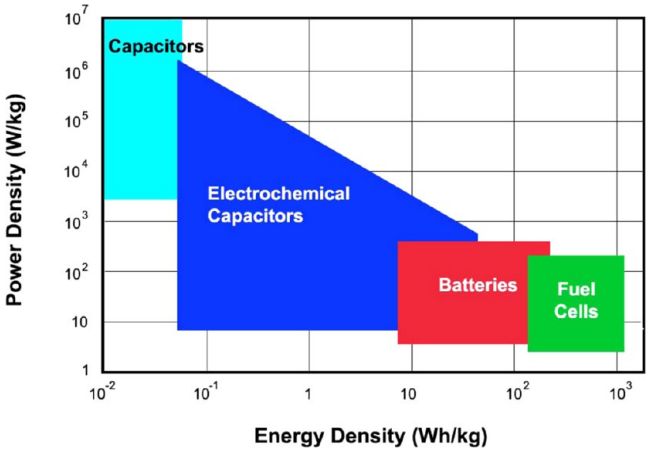

Figure 1. Supercapacitors are intermediate between batteries and capacitors in both energy and power density.

2.1.1. Electrochemical Capacitor Materials. The leading electrical energy storage technologies today are batteries and electrochemical capacitors. Both are based on electrochemistry and the power and energy relationship between the two is shown in a Ragone Plot (Figure 1). The success of lithium-ion batteries over the past two decades in consumer electronics and, more recently, the first generation of plug-in hybrids and fully electric vehicles, has led to a number of advances in energy-storage technology. Nonetheless, capacitive storage offers a number of desirable properties: fast charging (within seconds), reliability, long-term cycling (>500000 cycles), and the ability to deliver more than 10 times the power of batteries. Moreover, it is apparent that there are unique opportunities for ECs where batteries are simply not appropriate.[1] A good example is energy recovery where ECs are being used to recover energy from repetitive processes (descending elevators and braking cars), applications enabled by their fast charging rate.[2] The limiting feature that prevents more widespread usage of ECs has been the relatively low-energy density of the materials used in capacitive storage applications.

As mentioned previously, ECs may be divided into two main areas based on their energy storage mechanism: electric double layer capacitors (EDLCs) and pseudocapacitors.[4] The former is based on storing electric charge in a thin double layer at the interface between the electrode, typically carbon, and the electrolyte, while the latter involves reversible faradaic charge transfer. ECs make use of three main classes of materials: (1) carbon, (2) conducting polymers, and (3) metal oxides. The latter two are based on faradaic reactions. In a comparison among the three categories, RuO_2 is the most widely investigated metal oxide[3] (see also Quantum-Mechanical Studies of Supercapacitor Materials). In the following paragraphs, we briefly review EDLC and metal oxide pseudocapacitor materials.

Electrochemical Double Layer Capacitors. The physical nature of the capacitive charge storage mechanism for EDLCs (and ECs in general) differs significantly from that of batteries (chemical energy storage) and leads to certain advantageous operating characteristics. EDLCs have higher specific power than most batteries and their charge/discharge characteristics are highly reversible leading to cycle lifetimes in excess of 500000 cycles.[5] EDLCs can have extremely high specific capacitances; activated carbons typically have values ranging from 100 to 200 F/g.[6] Such values can be expected as the double layer capacitance is on the order of 10 μF/cm^2 for various carbons in aqueous electrolytes, and methods for developing carbons with high surface areas, in excess of 1500 m^2/g, are well-established.[5]

Although EDLCs have high-power capabilities, their energy density is well below that of batteries. The reason is that in contrast to batteries, there are no redox reactions and charge is stored at the surface of the electrode material (i.e., carbon). Thus, the charge can be quickly discharged or charged, but the amount of charge stored at the interface is limited. In recent years, there has been considerable effort aimed at increasing specific energy of EDLCs without compromising specific power and there are reports of energy density values reaching 10 Wh/kg.

Pseudocapacitor Materials. Redox-active pseudocapacitive materials are interesting for applications in electrochemical capacitors because the energy density associated with faradaic reactions is much higher, by at least an order of magnitude, than for traditional double layer capacitor materials (above 100 μF/cm^2 for pseudocapacitance versus 10 to 20 μF/cm^2 for EDLCs).[4] Thus, by creating high surface area pseudocapacitor materials, typically transition metal oxides because of their charge transfer properties,

dx.doi.org/10.1021/jp501047j | J. Phys. Chem. C 2014, 118, 19505−19523

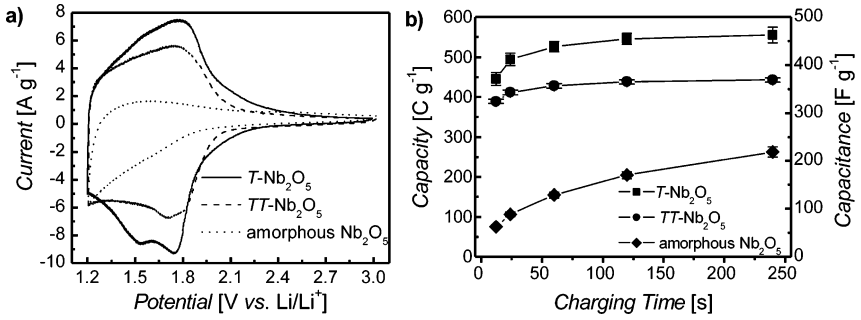

Figure 2. Voltammetric sweeps for Nb_2O_5 in lithium ion electrolyte: (a) CVs at 10 mV s^{-1} for different Nb_2O_5 phases (T-Nb_2O_5 is orthorhombic; TT-Nbb_2O_5 is pseudohexagonal) and (b) charge storage as a function of charging time for the same materials. The T-phase demonstrates the highest level of charge storage capacity for all sweep rates investigated.

it should be possible to greatly increase the specific capacitance to levels well above that of carbon.

The origin of pseudocapacitance has been described thoroughly by Conway.[7] In this description, pseudocapacitance occurs whenever the amount of charge insertion (Q) depends on the voltage (V), thus leading to a capacitance (Q/V). On the basis of this model, we identified three common charge storage processes that occur when a redox-active material is immersed in electrolyte. (1) Ions can intercalate into preferred crystallographic sites, often in materials characterized by layered or tunnel structures. The intercalation is diffusion limited and accompanied by metal valence change to preserve electrical neutrality. (2) Ions are electrochemically adsorbed onto the surface of the material. In this mechanism, referred to as redox pseudocapacitance, adsorption is associated with a change in the metal valence state. This process is kinetically facile because of the short-range nature of ion transport. (3) In our research, we have also observed mesoporous oxides in which intercalation is facile, giving rise to a capacitive response. This third process is referred to as intercalation pseudocapacitance.

Despite the advantages of having faradaic reactions, prior work with pseudocapacitive materials has brought to light an important question about reaching the very high theoretical values of the pseudocapacitive systems. The theoretical specific capacitance, based on either 1- or 2-electron redox reactions, is very high for systems such as V_2O_5, NiO, and MnO_2, well above 1000 F/g.[8−10] These high values have been demonstrated experimentally using nanoscale forms of these materials and specially designed electrode structures which ensure that most of the electrochemically active transition metal oxide participates in the reaction. However, standard composite electrode approaches are not as effective since specific capacitance values are typically in the range of 150 to 250 F/g.[11] Thus, one of the central issues we have been addressing in the MEEM program is the development of electrode architectures which retain high specific capacitances and offer a practical electrode structure for capacitor devices.

The MEEM program on capacitive energy storage is a comprehensive one which combines experimental and computational components to achieve a fundamental understanding of charge storage processes in redox-based materials, specifically transition metal oxide systems. As indicated above, these materials are a particularly appealing target because, with few exceptions, theoretical values of their specific capacitance are several times greater than experimentally achieved results. It is, therefore, a topic where improved fundamental understanding of pseudocapacitive materials can have a dramatic impact on the EC field. A central theme for the experimental studies is to create pseudocapacitor materials with appropriate nanoscale architecture. Accordingly, we have emphasized template-directed mesoporous transition metal oxides in which the interconnected pore network provides electrolyte access to the high surface area, electrochemically active walls. This architecture can also be used to promote the development of high conductivity pathways, thus facilitating charge transfer at the redox-active sites at or near the pore walls. A key issue with electrode architectures is the local electric field and the potential distribution at the pore-solid interface, and we have developed simulations to provide this information. Complementing these studies are first-principles calculations that elucidate the energies associated with the redox processes and help us to identify the features which contribute to high-performance energy storage materials.

2.2. Nb_2O_5: A Prototypical Intercalation Pseudocapacitor Material. Our initial studies of pseudocapacitor materials were based on using mesoporous films as discussed in Nanostructured Pseudocapacitive Materials below. This architecture enabled us to investigate the fundamental pseudocapacitor properties of various transition metal oxides under beneficial conditions: no binder or carbon additives, sufficiently thin films to provide adequate electronic conductivity, and interconnected mesoscale porosity to enable electrolyte access to redox-active pore walls.[12−15] In the course of the studies with MoO_3 and Nb_2O_5, we became aware that Li^+ diffusion in the film was extremely rapid. We now recognize that Nb_2O_5, in particular, has structural and electrochemical features that lead to intercalation pseudocapacitance, an extremely effective mechanism for storing high levels of charge rapidly.

Previous research had shown that Nb_2O_5 was able to reversibly intercalate Li^+ and protons and was investigated both as an electrochromic material and as a lithium-ion battery electrode.[16,17] However, the kinetics of this material had never been determined. The results with mesoporous films indicated that not only that Li^+ insertion was extremely rapid but also that mesoporous crystalline materials (orthorhombic T-phase) had much better kinetics and charge storage properties than the corresponding mesoporous amorphous films. In more detailed studies directed at the effects of crystallinity and phase on fundamental charge storage properties, we found that this material possesses much better charge storage kinetics than other transition metal oxides.[18] The orthorhombic phase, in particular, was found to exhibit high specific capacitance at high rate with values of nearly 450 F/g achieved in less than 1 min. This behavior is shown in Figure 2. It is evident that the amorphous phase has much slower kinetics and less charge storage than either of the crystalline phases. This great difference is an indication of how faradaic processes which occur in crystalline materials lead to an additional capacitive component which does

dx.doi.org/10.1021/jp501047j | J. Phys. Chem. C 2014, 118, 19505−19523

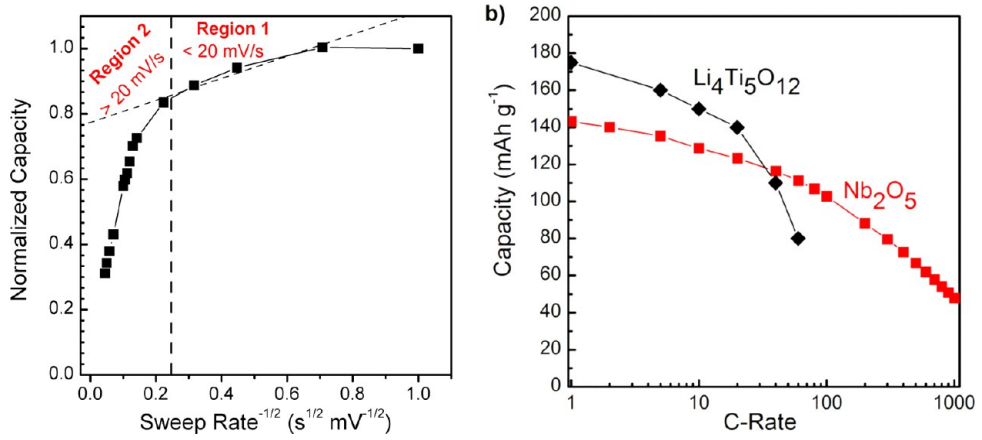

Figure 3. (a) Capacity vs $\nu^{-1/2}$ allows for the separation of diffusion-controlled capacity from capacitive-controlled capacity; two distinct kinetic regions emerge when the sweep rate is varied from 1 to 500 mV s^{-1}. The dashed diagonal line corresponds to the extrapolation of the infinite sweep rate capacitance using the capacity between 2 and 20 mV s^{-1}. (b) Comparison of the rate capability of *T*-Nb_2O_5 with a high-rate lithium-ion anode, $Li_4Ti_5O_{12}$, at various C-rates. Reprinted with permission from ref 20. Copyright 2013 Nature Publishing Group.

not occur with noncrystalline materials. In evaluating the kinetics of charge storage, we used an approach first used by Trasatti et al.[19] in which one identifies the infinite-sweep rate capacity, which relates to the specific capacitance obtained at high rates. The values for Li^+ insertion in orthorhombic Nb_2O_5 are much greater than that of birnessite MnO_2 (400 vs 270 F/g), another well-known pseudocapacitive material. Moreover, these infinite-sweep rate capacity values are quite comparable to those of RuO_2 (480 F/g), even though the pseudocapacitive charge storage mechanisms are different. That is, Nb_2O_5 stores charge at high rates from Li^+ insertion, whereas charge storage with RuO_2 and most other transition metal oxides is based on redox reactions occurring at the surface and near-surface regions.

In more recent work, we were able to attribute the high level of energy storage at high rates in Nb_2O_5 to an intercalation pseudocapacitance mechanism.[20] The characteristic features of this mechanism include currents which vary inversely with time, charge-storage capacity that is mostly independent of rate, and redox peaks that exhibit small voltage offsets, and therefore good reversibility, at high rates. Kinetic studies indicate that solid-state lithium-ion diffusion is rate-limiting but only for charging times below 20 s. Moreover, with somewhat longer charging times of 1 min, there are no indications of diffusion limitations and the current response is capacitor-like (Figure 3a).[20] First-principles calculations based on the density-functional theory (DFT) (see Quantum-Mechanical Studies of Supercapacitor Materials) show that migration energies for Li^+ ions in *T*-Nb_2O_5 are very low and show a pronounced structural disorder which is caused by partial Nb occupations on the 4*f* sites, in agreement with our experimental charging data. Another key design rule for intercalation pseudocapacitance is that the structure does not undergo a phase transformation upon intercalation. In the case of Nb_2O_5, facile two-dimensional (2D) pathways seem to be important; charge storage in such a 2D environment would then exhibit similar behavior to 2D surface adsorption reactions identified by Conway.[7] Finally, the results shown with Nb_2O_5 are exciting because they demonstrate that even with charging times as fast as 1 min (60C), charge storage in the material is not limited by solid-state lithium-ion diffusion.

Because the high rate properties of Nb_2O_5 are due to fast ion diffusion in the bulk material, and not the surface area, the intercalation pseudocapacitance mechanism may be very useful in the development of thick electrodes capable of storing significant amounts of energy. Accordingly, we investigated this feature by fabricating 40 μm thick electrodes, using composite approaches of the type that would be utilized in electrochemical capacitor devices.[20] In Figure 3b, a Nb_2O_5 electrode is compared with that of $Li_4Ti_5O_{12}$, a well-known high-rate lithium ion battery material. A crossover point occurs at about 40C, as the rate capability for Nb_2O_5 becomes significantly better than that of $Li_4Ti_5O_{12}$ above this discharge rate.

In summary, our studies with Nb_2O_5 indicate that this material is a very promising one for electrochemical energy storage. Charge storage in this material is attributed to intercalation pseudocapacitance in which faradaic reactions occur within the bulk, rather than being confined to the surface and near surface regions as occurs with the well-known pseudocapacitor materials. The material exhibits high capacity at high discharge rates with values comparable to or better than the best high-rate battery material, $Li_4Ti_5O_{12}$. Because the high rate capability of Nb_2O_5 is due to fast ion transport in the bulk material, this mechanism may be very attractive for thick composite electrodes because the need to expose the surface to the electrolyte is less critical.

2.3. Nanostructured Pseudocapacitive Materials. Significant fraction of our research in the MEEM program has focused on creating materials with structures optimized for pseudocapacitive charge storage.[21] In particular, we have emphasized the careful control of nanometer scale architecture because of the ability to obtain short diffusion distances which are useful for charge storage processes. For pseudocapacitor materials, we hypothesize that an ideal structure should contain interconnected porosity on the 10−30 nm length scale to facilitate electrolyte diffusion through the material and enable electrolyte access to redox active sites, have inorganic domains with sizes between 5 and 20 nm to facilitate ion adsorption, and to keep ion transport distances short.

A broad range of suitable structures can be created using diblock copolymer templating.[22−25] The general method is depicted in Figure 4. In this process, inorganic building blocks coassemble with an amphiphilic diblock copolymer. Sol−gel chemistries are well-suited for such polymer-templating techniques. In a typical synthesis, inorganic precursors, often metal alkoxides or metal salts, are codissolved with the organic block copolymer and then cast onto a substrate, either through dip-coating, spin-coating, or drop-casting. The micelles then coassemble with the inorganic precursors into cubic or hexagonal

dx.doi.org/10.1021/jp501047j | J. Phys. Chem. C 2014, 118, 19505−19523

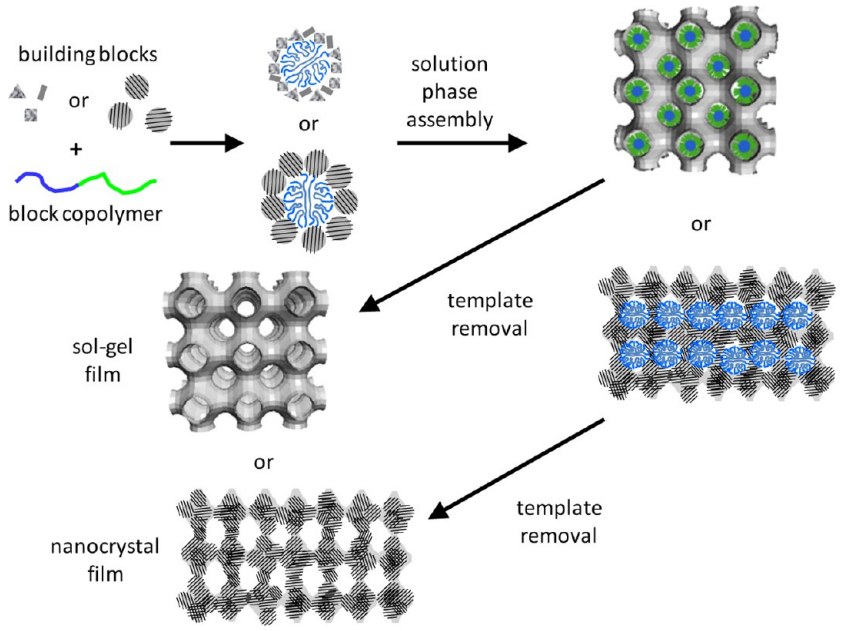

Figure 4. Evaporative-induced self-assembly process for producing cubic mesoporous films. The building blocks can be either molecular precursors leading to sol−gel-based films or preformed nanocrystals, leading to nanocrystal-based films.

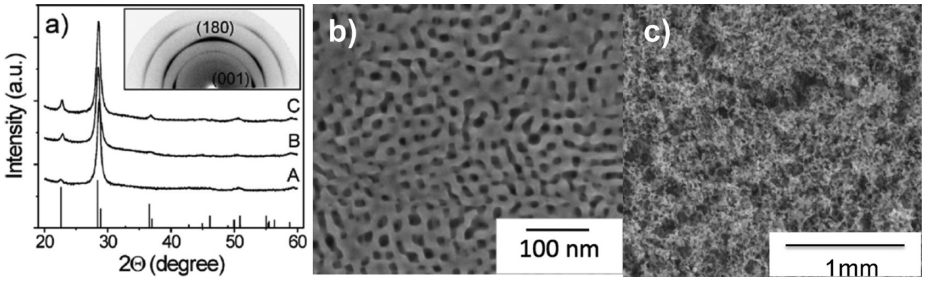

Figure 5. (a) 1D-WAXD data obtained on polymer-templated (A) *T*-Nb_2O_5, (B) *L*-Ta_2O_5, and (C) $TaNbO_5$ films. The stick pattern shows orthorhombic *T*-Nb_2O_5 according to the JCPDS reference card no. 30-0873. A typical 2D-WAXD pattern for mesoporous *T*-Nb_2O_5 is shown in the inset of (a). (b) SEM image of a polymer-templated porous niobia film. (c) SEM image of a porous niobia film made using PMMA colloids.

structures as the inorganic precursors undergo hydrolysis and condensation reactions. The dry film can then be heated to decompose the polymer template and further condense/crystallize the inorganic framework, leaving behind the desired mesoporous film.

Figure 5b shows a scanning electron microscope (SEM) image of a sol−gel derived nanoporous Nb_2O_5 film that was crystallized at 600 °C.[13] The film is macroscopically homogeneous with a network of open pores averaging 13−15 nm in diameter. The film was templated with poly(ethylene-*co*-propylene)-*b*-poly(ethylene oxide), or PEP−PEO. A unique property of these large block copolymers, when compared to surfactants and small pluronic type polymers, is their ability to produce porous inorganic materials with fairly thick pore walls. During heating of a film with thick walls, crystallites can nucleate with a critical domain size that is smaller than the pore wall. Nucleation and grain-growth can then both occur within the oxide wall, leading to crystalline, yet ordered mesoporous structures.

Most crystalline, polymer-templated mesoporous materials contain randomly oriented nanoscale domains with sizes on the order of the average wall thickness. Nanoporous niobia, however, shows very different crystallization behavior. With templated, porous Nb_2O_5, the substrate appears to have a very strong influence on the crystallization kinetics, and the result is a film that exhibits a high degree of crystallographic orientation relative to the substrate. Figure 5a shows wide-angle X-ray diffraction (WAXD) data collected on mesoporous *T*-Nb_2O_5, *L*-Ta_2O_5, and $TaNbO_5$.[13] The films show only one distinct peak, the (180) reflection, for all three samples, indicating a highly textured film with the primary layer direction running parallel to the substrate. Similar iso-oriented films have been observed for mesoporous MoO_3, and in that system, the orientation appears to have a significant and positive effect on the electrochemical rate capability.[15]

To create smaller crystalline domains with smaller Li^+ diffusion distances and higher surface areas, we turn to a new route for making porous materials−nanoporous films made from preformed nanocrystal building blocks (Figure 4).[12,26−30] Templated nanocrystal-based materials show much higher surface areas than the sol−gel-derived systems discussed above and are thus an ideal way to build redox pseudocapacitance into a material. Because micropores are created at the intersections between nanocrystals, the electrolyte can penetrate into the pore wall, creating much shorter diffusion distances. These very small domain sizes can be important for creating high-capacity pseudocapacitive materials.

The key to replacing sol−gel precursors with preformed nanocrystals is to create soluble, but ligand free, nanocrystals.

dx.doi.org/10.1021/jp501047j | *J. Phys. Chem. C* 2014, 118, 19505−19523

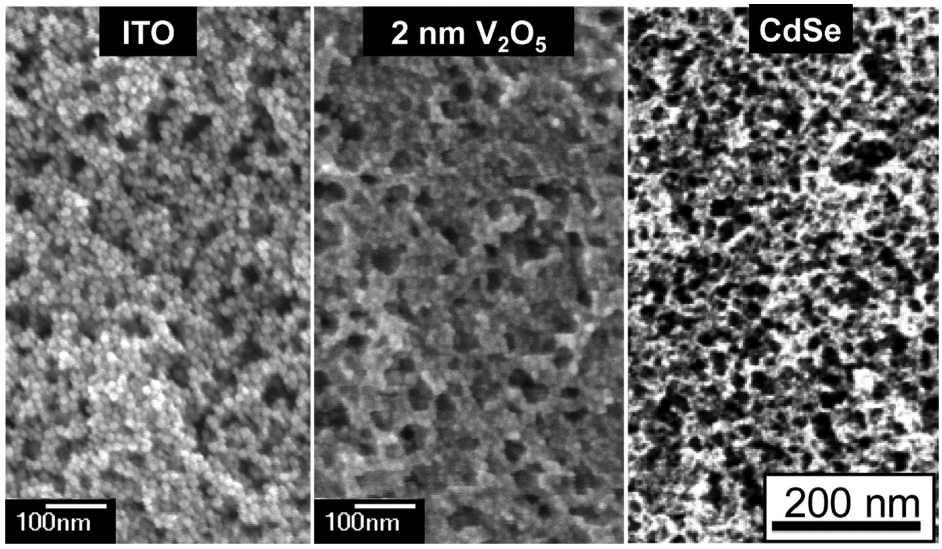

Figure 6. SEM images of porous materials synthesized using block copolymer templating of preformed, ligand-stripped nanocrystal building blocks. Materials are (a) ITO, (b) ITO coated with 2 nm of vanadia, and (c) CdSe.

Initial work on polymer-templated nanocrystal-based films made use of nanocrystals with hydrolyzable ligands that were metastable in solution.[12,29,30] More recently, we have developed robust and transferable synthesis methods that use stable, charge-stabilized nanocrystal solutions with chemically stripped ligands.[31] Figure 6a shows an SEM image of a nanocrystal-based nanoporous film made from ligand stripped indium tin oxide (ITO) nanocrystals.[26] While ITO itself is not a redox active material, similar films can be made from a range of redox active oxides, including Mn_3O_4, $(Mn,Fe)_2O_3$, and TiO_2 among others.[26,32] ITO is shown here because the highly conductive nature of ITO allows for very clear SEM images in which the pores and individual nanocrystals can both be resolved. These porous ITO films can also serve as scaffolds for composite electrode materials in which the conductive ITO film is coated with a redox-active material such as V_2O_5 (Figure 6b).Vanadia-coated ITO shows nearly 100% pseudocapacitive charge storage for thin vanadia layers. This architecture also allows us to define the vanadia coating thickness, where the current becomes diffusion controlled rather than having a capacitor-like response. Nonoxide porous materials can also be produced using these methods.[27,33] For example, Figure 6c shows a nanoporous CdSe film produced using ligand stripped CdSe nanocrystals.[27] The extension of these methods to nonoxide systems opens up a wide range of applications in both electrochemical charge storage and in other fields.

The systems described above are ideal test beds for understanding pseudocapacitive charge storage as they are binder free, fully electrically connected networks that are sufficiently thin that electrical conductivity is usually not rate-limiting. To transition these materials toward practical electrodes, we have recently developed methods to produce porous niobia films using poly(methyl-methacrylate) (PMMA) colloids,[34,35] in combination with niobia polyoxometalate (POM) clusters.[36,37] Figure 5c shows an SEM image of a porous POM-derived film. The pores size, the wall thickness, and the overall film thickness are highly tunable in these porous niobia films.

2.4. Quantum-Mechanical Studies of Supercapacitor Materials. First-principles calculations based on the density-functional theory (DFT) are well-suited for the task of understanding the microscopic mechanisms of EC pseudocapacitance and how they relate to the intrinsic properties of the material. Here we review two prototypical cases, hydrous ruthenia ($RuO_2{\cdot}xH_2O$) and crystalline MoO_3. Comparison of these materials provides insights into the main physical and chemical features characterizing high-performance EC materials.

Ruthenium dioxide (RuO_2), a prototypical EC electrode with one of the highest specific energy densities of all known materials (values in the range of 800 F/g have been reported for hydrous $RuO_2{\cdot}xH_2O$),[38,39] is a remarkable stoichiometric oxide which combines metallic conductivity, chemical stability, and the ability to support redox reactions.[40,41] Anhydrous RuO_2 crystallizes in the rutile TiO_2-type structure shown in Figure 7a, which is

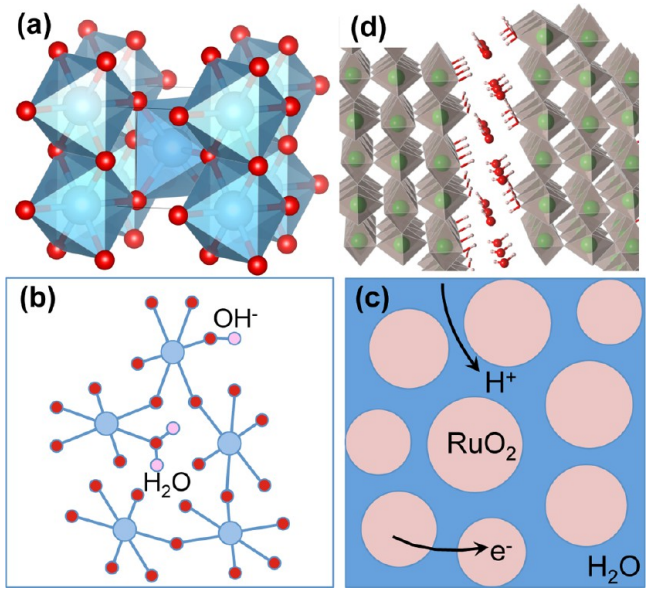

Figure 7. (a) Tetragonal rutile-type crystal structure of RuO_2. Tetragonal axis is oriented along the vertical direction. Schematic (b) "water in bulk vacancies" and (c) "water at grain boundaries" structural models proposed for hydrous $RuO_2{\cdot}xH_2O$. (d) A typical low-energy structure for $RuO_2{\cdot}H_2O$ found by DFT. Water molecules aggregate in a layer between slabs of crystalline RuO_2, resembling the "water at grain boundaries" model shown in panel (c).

dx.doi.org/10.1021/jp501047j | J. Phys. Chem. C 2014, 118, 19505−19523

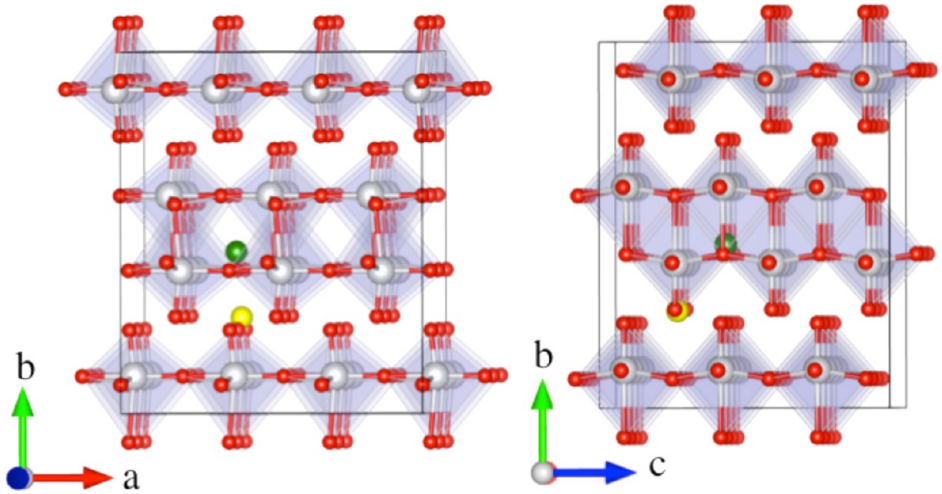

Figure 8. Lithium intercalation sites in orthorhombic α-MoO_3 along (001) (left panel) and (100) (right panel) directions. Mo (white) and O (red) octahedra are outlined, as well as the intralayer (green) and interlayer (yellow) lithium sites.

characterized by chains of edge-sharing RuO_6 octahedra running along the tetragonal direction. These chains are linked together by sharing corners. The calculated electronic structure shows that the bonding hybrids of O 2p and Ru 4d orbitals lie 2 to 8 eV below the Fermi level, while the antibonding p−d hybrids are above the Fermi level. The metallic conductivity of RuO_2 is attributed to delocalized states formed by overlapping Ru 4d orbitals across the shared edges of RuO_6 octahedra.[42] In accordance with the conventional point of view, charge storage in RuO_2 occurs according to the following electronic-protonic double insertion reaction:[43]

$$RuO_x(OH)_y + \delta e^- + \delta H^+ \leftrightarrow RuO_{x-\delta}(OH)_{y+\delta} \quad (1)$$

where the valence state of individual Ru ions changes from Ru^{4+} to Ru^{3+} and even Ru^{2+}. In our DFT studies, we find a more nuanced picture of chemical bonding where electron−proton double insertion leads to the formation of a polar covalent O−H bond with a fractional increase of charge in the Ru d states by only 0.3 electrons. This fractional change in the Ru valence can be attributed to the delocalized (metallic) nature of the Ru 4d states near the Fermi energy.[42] Furthermore, DFT studies indicate that fast reversible adsorption of up to 1.5 protons per Ru on the (110) surface contributes to the pseudocapacitive current, while the current associated with proton intercalation into bulk RuO_2 is diffusion-limited and depends strongly on the charging rate.[44,45] Hence, the latter is not expected to contribute to pseudocapacitive behavior.

It is well-known that hydrous ruthenia, $RuO_2{\cdot}xH_2O$,[46] shows far superior pseudocapacitive performance in comparison with nanocrystalline anhydrous RuO_2 films.[39] This is usually attributed to the mixed protonic and electronic conductivity of the former. However, the structure of hydrous ruthenium, which holds the key to describing the transport pathways for electrons and protons, is not well-characterized. Two distinct structure models have been discussed in the literature.[38] The first model assumes that water molecules are incorporated in ruthenium vacancies in the bulk material as shown in Figure 7b; we call this the "water in bulk vacancies" model. The second model ("water at grain boundaries") assumes that water is dispersed between RuO_2 nanocrystals, and the material can be best-described as an RuO_2/H_2O composite held together by boundary layers of structural water (see Figure 7c).[47] To clarify the energetic tendencies, we have used the prototype electrostatic ground state (PEGS) search method[48,49] in conjunction with DFT calculations to investigate low-energy structures of hydrous ruthenia. Our results show that incorporation of water in Ru vacancies or in bulk crystals is energetically much more costly than segregation of water molecules between slabs of crystalline RuO_2 (as shown in Figure 7d).[45] These results lend support to the "water at grain boundaries" model for the structure of hydrous $RuO_2{\cdot}xH_2O$, confirming the picture that emerges from recent experimental work.[39,50−52] The superior charge storage properties of hydrous ruthenia are then attributed to the resulting composite structure, which facilitates fast electronic transport through the metallic RuO_2 nanocrystals and fast protonic transport through the regions of structural water at grain boundaries (see Figure 7). The small radii of the RuO_2 nanocrystals (down to a few nanometers) provides an enormous surface area for reversible proton adsorption, which accounts for the large pseudocapacitive currents observed experimentally in hydrous ruthenia.

Layered transition metal oxides, such as MoO_3, are attractive EC materials due to their ability to intercalate high concentrations of ions, and the potential for fast ion transport within their interlayer (van der Waals) gaps.[13,15] A prototypical example is the α-MoO_3 compound, the structure of which is illustrated in Figure 8. The structure is composed of MoO_6 octahedra that are edge-shared along the *c* axis, and corner shared along the *a* axis, to form MoO_3 bilayers that are oriented normal to the *b* axis and are bound by van der Waals forces. Each octahedron in the bilayers is equivalent by symmetry and characterized by a highly distorted geometry featuring five distinct metal−oxygen bonds, with bond lengths ranging between 1.63 and 2.30 Ångströms at room temperature.[53,54] The resulting structure has two distinct types of sites for intercalation of Li ions: one located within the one-dimensional intralayer channels that run parallel to the *c* axis (c.f. the green sphere in Figure 8) and the other in the two-dimensional interlayer "van der Waals gap" regions normal to the *b* axis (c.f. the yellow sphere in Figure 8).

First-principles calculations of the relative energetics of the interlayer versus intralayer sites have been investigated within the framework of van der Waals corrected DFT,[55,56] including Hubbard-U corrections[57] with a *U* parameter having a value of 6 eV. The inclusion of Hubbard-U corrections ensures that the extra electron introduced by Li intercalation is localized as

dx.doi.org/10.1021/jp501047j | J. Phys. Chem. C 2014, 118, 19505−19523

small-polarons on the Mo cations (converting a nominal Mo^{6+} ion to Mo^{5+}), as observed experimentally for dilute concentrations.[58,59] In calculations with fixed lattice constants we find that the intralayer site is preferred energetically when the intercalated Li ion is bound to a nearest-neighbor electron small polaron. However, the energetic preference for this site relative to the interlayer van der Waals gap position is relatively small (less than 0.1 eV), and influenced by a higher polaron binding energy. Specifically, for calculations with fixed lattice constants the site preference switches to the interlayer site when the electron small polaron lies far from the Li ion. Further calculations have been undertaken with the aid of two different vdW-corrected density functionals to investigate the effect of relaxations of the supercell lattice parameters in influencing Li intercalation energetics. It is found that relaxations have relatively small effects on the calculated Li-polaron binding energies. However, one functional predicts that the interlayer site is stabilized relative to the intralayer site by lattice parameter relaxations, both with and without polaron binding, while the other predicts relatively smaller effects on site preferences due to such relaxations. Overall, the calculations suggest that the energetics of Li intercalation are influenced by a subtle interplay of competing thermodynamic effects including strain energy and entropy (which favors dissociation of Li-polaron pairs), and that their balance will be affected by temperature and particle size effects.[60]

2.5. Multiscale Modeling of Supercapacitors. In the MEEM program, we have developed rigorous physical modeling and accurate numerical tools to facilitate the design and optimization of the electrode morphology for electrochemical capacitors (ECs). Physical modeling of supercapacitors is made difficult by the different and intimately coupled interfacial and transport phenomena taking place in the device such as (i) charge transport in the electrodes, (ii) ion transport in the electrolyte under the combined effects of electric field and concentration gradient, (iii) redox reactions, (iv) ion insertion in the electrode, (v) local heat generation, and (vi) thermal energy transport. Another challenge in modeling supercapacitors is their multiscale nature and their complex porous electrode morphology with ions on the order of 1 nm in diameter, pore diameters ranging from 1 to 100 s of nanometers, electrodes of 0.1−10 μm thick, and devices approximately 1−10 mm in size.

In developing our models, several features needed to be considered properly. First, the finite ion size and the Stern layer must be taken into account.[61] Indeed, the ions have finite size and their concentration at the electrode surface cannot exceed a maximum concentration, often taken as simple cubic ion close packing. The Stern layer refers to the compact layer of ions strongly adsorbed to the electrode surface. There are no free charges within the Stern layer, and its thickness is typically taken as the effective radius of an ion. Second, the electrolyte dielectric permittivity can no longer be treated as constant but instead decreases with increasing electric field.[61] Indeed, the electric field at the electrode surface can be very large, particularly for large surface curvature. As a result, the local electrolyte polarization becomes saturated and the dielectric permittivity decreases. This phenomenon can be successfully captured by the Booth model,[62,63] as confirmed by both experimental measurements and molecular dynamic simulations.[64]

2.5.1. Equilibrium Models. The modified Poisson−Boltzmann (MPB) model[65,66] is an equilibrium model governing the local equilibrium electric potential while ion concentrations are given by the Boltzmann distribution. In adapting this model, a set of new boundary conditions was derived for cylindrical and spherical electrode particles or pores to account for the very thin Stern layer without simulating it in the computational domain.[67] This greatly simplified the simulations by significantly reducing the necessary computing resources and time without affecting accuracy. In fact, these new boundary conditions made possible the simulation of electric double layer capacitors (EDLCs) with three-dimensional (3D) porous electrodes. They were used to faithfully simulate actual electrodes of EDLCs, consisting of ordered bimodal mesoporous carbon featuring both macropores and mesopores.[68] This comparison is shown in Figure 9. The new

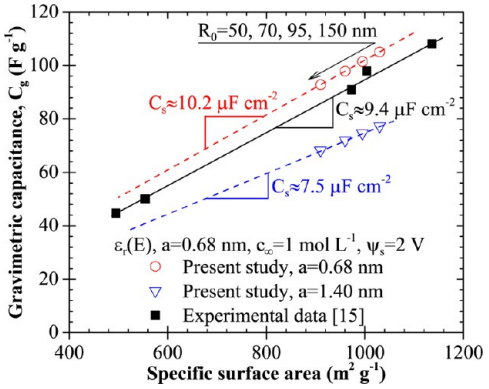

Figure 9. Predicted and experimentally measured gravimetric capacitance (C_g) for bimodal porous carbons as a function of their specific surface area. The upper and lower bounds are based on using solvated and nonsolvated diameters for the electrolyte ions. Reprinted from *J. Power Sources*, 221, Wang, H. N.; Pilon, L. Mesoscale Modeling of Electric Double Layer Capacitors with Three-Dimensional Ordered Structures, 252−260, 2013 with permission from Elsevier.

boundary conditions can also be employed to simulate the dynamic charging and discharging of EDLCs as well as pseudocapacitors.

Detailed numerical simulations can be used to simulate highly ordered porous structures whose symmetry helps reduce the computational domain size. However, numerous electrodes feature complex disordered structures with pores of various shapes and sizes. To treat this situation, scaling analysis was performed to reduce a large number of design parameters to a few meaningful dimensionless similarity parameters accounting for the dominant physical phenomena governing the behavior of actual electrodes.[69] These dimensionless numbers were applied to experimental data for equilibrium integral capacitance of EDLCs with porous carbon electrodes with a wide range of morphology and different binary electrolytes. In this way, we were able to develop design rules to maximize the capacitance of EDLCs: (i) the electrolyte should have small ions and large dielectric constant and (ii) the electrode pore radius should be tailored to closely match the ion radius, and (iii) the pore size distribution should be as narrow as possible.

2.5.2. Dynamic Models. The Modified Poisson−Nernst−Planck (MPNP) model[70] governs the time-dependent local ion concentrations and electric potential in binary and symmetric electrolytes. We have recently solved these equations to numerically reproduce typical (i) cyclic voltammetry (CV),[71] (ii) impedance spectroscopy,[72,73] and (iii) galvanostatic cycling[74] measurements. One particularly useful example which illustrates our contributions is our providing a physical explanation for a CV-feature (a "hump" in the CV curve), which had baffled the experimentalists. Our interpretation was that the hump occurred because of "crowding" of the electrode surface with ions of finite

size.[71] In other words, the current reaches a maximum when the ion surface concentration approaches its maximum.

The MPNP model is limited to binary and symmetric electrolytes defined by two ion species having identical size, valency, and transport properties. Common electrolytes, however, are asymmetric (e.g., aqueous H_2SO_4 and Na_2SO_4 or $LiClO_4$ in polycarbonate). Moreover, the use of electrolyte mixtures with more than two ion species has recently been considered to increase the energy and power densities of supercapacitors. To be able to simulate asymmetric electrolytes, we derived a generalized modified Poisson-Nernst-Planck (GMPNP) model from first-principles based on excess chemical potential and the Langmuir activity coefficient.[75] The model was used to simulate CV measurements for binary asymmetric electrolytes in EDLCs. The results demonstrated that the current density increased significantly with decreasing ion diameter and/or increasing valency of either ion species. In contrast, the ion diffusion coefficients affected the CV curves and capacitance only at large scan rates. Scaling analysis was also performed on the GMPNP model.[75] The similarity parameters obtained accounted for the dominant physical phenomena in the asymmetric electrolytes and in the electrode. A self-similar behavior was observed for the capacitance of the device as a function of scan rate. Diffusion-independent and diffusion-limited regimes were identified along with the associated transition criteria.

Overall, we have advanced significantly the state-of-the-art in physical modeling and simulations of supercapacitors by developing new boundary conditions that rigorously account for interfacial phenomena at the electrode/electrolyte interface and enable the simulations of actual 3D mesoporous electrodes. Transport model for asymmetric electrolytes and electrolyte mixtures was also derived from first principles. The developed numerical tools were able to numerically reproduce experimental measurements and to provide physical interpretations for experimental results. Scaling analysis was systematically performed and the resulting similarity parameters reduced the number of variables and were used to identify self-similar behavior, diffusion-limited operation, and design rules for both electrodes and electrolytes.

3. SOLUTION PROCESSED ORGANIC PHOTOVOLTAICS

3.1. Avoiding Kinetic Control over the Morphology of Organic Photovoltaic Devices. In recent years, dramatic progress has been made in the field of organic photovoltaics (OPVs), with the power conversion efficiencies of polymer/fullerene devices surpassing 10%.[76] Nearly all of the increase in power conversion efficiency comes from devices fabricated with the blend cast (BC) method, in which the polymer donor and fullerene acceptor are randomly mixed together in solution and then cast into a film to form the active layer of the organic solar cell. The problem with BC processing is that the two components must be blended together on a fine enough length scale (usually considered to be ~10 nm[77]) to ensure efficient charge separation, but must also be phase-separated enough that each component forms a connected network that is able to efficiently transport the separated charges to their respective electrodes.[78,79] When the two components start blended together in solution, the morphology of the film cast from the solution is dictated by the donor/acceptor miscibility, the propensity of one or both materials to crystallize, the relative solubilities of the two materials in the solvent from which the film is cast, the drying kinetics of the film for the given casting conditions, etc. This means that the nanometer-scale morphology, and thus, the device performance, is hypersensitive to the processing kinetics used to make a BC film. To try to improve control over the nanometer-scale morphology of BC films, researchers in the field use techniques such as postfilm deposition thermal annealing,[80−82] slow drying during film formation,[83−85] postdeposition solvent annealing,[86,87] and the use of solvent additives during processing.[88−90] Unfortunately, this means that for any new set of OPV materials, the size of the processing parameter space to explore is large, necessitating an Edisonian approach to find the processing conditions that lead to the best device performance. Even worse than the fact that hundreds of BC devices must be fabricated when going through the trial-and-error process to optimize a new set of materials for solar cell efficiency is the fact that what works for small area (typically a few mm^2) devices on the laboratory scale is unlikely to work for larger-area (>cm^2) devices that would be manufactured industrially. This is because the formation kinetics of large-area films through techniques such as roll-to-roll processing or doctor blading are not the same as the spin-coating typically used at laboratory scales, resulting in poor efficiencies upon scale-up of the device area.[91]

At the UCLA-based MEEM center, we have worked to avoid this need for trial-and-error in device performance by developing methods that produce polymer/fullerene active layers whose nanometer-scale morphology is not sensitive to the kinetics of how the films are processed. Over the past few years, we have focused on two approaches for producing polymer/fullerene blend films with a morphology that is scale-independent. The first approach is to take advantage of molecular self-assembly to produce films with a nanometer-scale structure that is dictated more by the thermodynamics of the molecular assembly than the kinetics of the processing conditions. To this end, we have worked both with fullerenes that self-assemble because of a molecular propensity to form 1D stacks[92−95] and with conjugated polyelectrolytes that form micellar rods with improved polymer conductivity.[96] Our second approach is to use more traditional materials but to avoid the kinetic sensitivity issues with the BC method by sequentially processing the donor and acceptor layers. In this way, we can separately control the structural aspects of both the polymer and fullerene during deposition, producing morphologies that are different than those that can be obtained by simply blending the materials together in solution from the beginning[97−100] and which can survive being scaled-up in device area.

3.2. Using Self-Assembly to Control Organic Photovoltaic Morphology. *3.2.1. Self-Assembling Fullerenes to Control Global versus Local Electron Mobility.* The first approach taken by the MEEM center to avoid the sensitive processing kinetics that make it difficult to obtain a reproducible BC morphology in conjugated polymer/fullerene-based solar cells is to use self-assembling fullerenes that prefer to form molecular wires on the nanometer-length scales important for device performance. The self-assembling fullerene system to which we have devoted most of our focus is a series of 6,9,12,15,18-pentaaryl-1-hydro[60] fullerene molecules,[101] whose chemical structures are shown in Figure 10. Because of the molecular shape of these fullerene derivatives, we refer to them colloquially as "shuttlecocks" (SCs). One of the advantages offered by the pentaaryl substitution pattern is that simple alterations of the alkyl groups on the ends of the aryl "feathers" of these molecules changes the propensity for them to assemble into stacks without altering any of the electronic properties of the fullerene ball.[92] For example, the use of *t*-butyl phenyl alkyl groups (**1a**) leads to SCs that strongly prefer to assemble into 1D

dx.doi.org/10.1021/jp501047j | J. Phys. Chem. C 2014, 118, 19505−19523

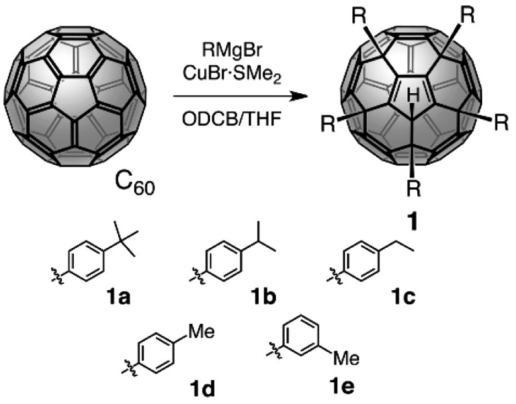

Figure 10. Chemical structures of the 6,9,12,15,18-pentaaryl-1-hydro[60]fullerenes ("shuttlecocks") synthesized for the MEEM center OPV effort.

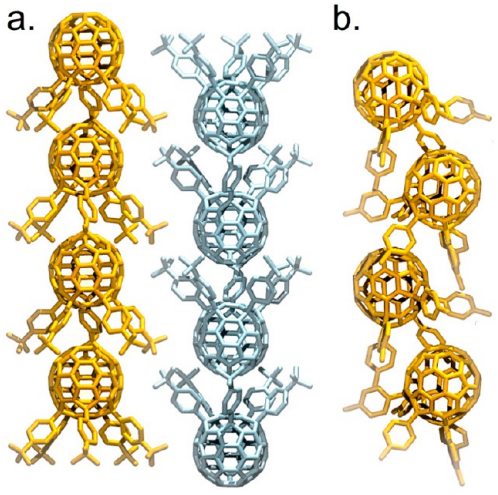

Figure 11. Crystal structures showing the ball-in-cup stacking motif of (a) (**1a**) and the nonstacked packing of (b) (**1d**).

stacks, as evidenced by the crystal structure shown in Figure 11a.[92,94] In contrast, the use of methyl alkyl groups (either in the para (**1d**) or meta (**1e**) positions) produces SCs that have no preference to stack ball-in-cup, as shown by the crystal structure of **1d** in Figure 11b. Ethyl (**1c**) and isopropyl (**1b**) substituents lead to intermediate behavior in the preference to stack.[94]

To understand how tuning the ability to form self-assembled stacks affects the properties of OPV devices based on these materials, we blended all of the SC molecules whose structures are shown in Figure 10 with poly(3-hexylthiophene 2,5 diyl) (P3HT). We found that the SCs that preferred to stack (**1a**,**1b**) produced solar cells with much higher power conversion efficiencies than those based on the SCs that do not stack (**1c**−**1e**), as shown in Figure 12a.[93] We observed via X-ray diffraction, atomic force microscopy (AFM) and photoluminescence (PL) quenching experiments that the nonstacking SCs had a greater degree of phase segregation from the P3HT than the stacking SCs, which produced more intimate blends.[93] Thus, to verify that the differences we observed in device performance were a result of the self-assembly of the fullerene stacks rather than different degrees of phase separation, we also constructed diodes out of the pure SC materials. Figure 12b shows current−voltage curves for diodes fabricated from **1a** and **1d**; the results (and our space-charge-limited mobility analysis of the data[95]) clearly show that for otherwise electronically identical molecules, fullerenes that stack have a much

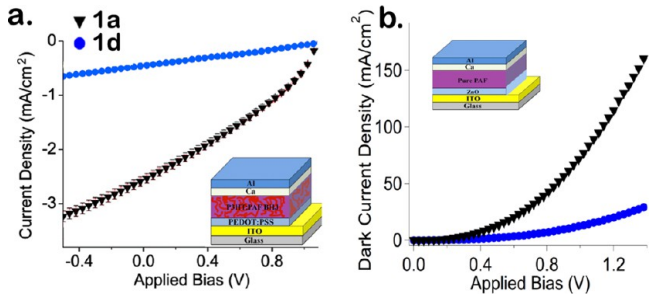

Figure 12. (a) J−V curves of P3HT:SC BC devices under 1 sun illumination. (b) J−V characteristics of electron-only diodes constructed from SC-only active layers. In both panels, ▲ show data for devices with **1a** and blue ● for devices made with **1d**.

higher carrier mobility than fullerenes that do not stack. Thus, the photovoltaic performance of devices based on self-assembling fullerenes such as **1a** are better than those of nonassembling fullerenes such as **1d** both because the nonstacking fullerenes phase segregate enough to lead to poor exciton harvesting and because the stacking fullerenes have an intrinsically higher mobility over device length scales, a direct consequence of their self-assembly.

Although the data presented above makes clear that fullerene self-assembly improves solar cell power conversion efficiencies, devices based on our SC fullerenes are still outperformed by standard, nonassembling fullerenes such as [6,6]-phenyl-C 61-butyric acid methyl ester (PCBM). To understand why nonassembling fullerenes like PCBM produce even higher currents in solar cells with P3HT than stacking SC molecules, we developed a new theoretical formalism to determine the rate of electron transfer between neighboring fullerenes in a photovoltaic device. Our formalism is built on the Marcus theory of electron transfer,[102] and we determined the electronic coupling via a density functional theory calculation of an isolated pair of fullerene molecules. To ensure that the excited Kohn−Sham orbitals in our calculation did not artificially localize on one of the two molecules, we also applied an external electric field to delocalize the excited state, mimicking the effects of the complex environment inside a photovoltaic device. The details of our method are given in ref 95. When we applied this formalism to the SCs of Figure 10, we found that the electron transfer rate between molecules is similar for the stacking and nonstacking SC molecules. Thus, the fact that these molecules are electronically identical means that their local, molecular rate of electron transfer is also similar, verifying that any differences in device performance must come from the assembly induced stacking on more macroscopic length scales. We also note, however, that the pentaaryl functionalization motif of these SC fullerenes leads to reduced electron density of the LUMOs of these molecules near the aryl substituents, limiting the electronic coupling between them, as shown in Figure 13b. This means that regardless of their ability to stack, there is a relatively poor rate of electron transfer between neighboring SC fullerenes. PCBM, in contrast, has only a single substituent on the fullerene cage that does not interfere with the delocalization of the LUMO, as shown in Figure 13a; this provides for good electronic overlap between neighboring PCBM molecules regardless of orientation, facilitating electron transfer in all directions. Thus, PCBM outperforms the self-assembling SC fullerenes (and indeed most other fullerenes that have been tried in organic photovoltaics) because it has enhanced nearest-neighbor electronic overlap, and thus high carrier mobility on local, molecular length scales.[95]

dx.doi.org/10.1021/jp501047j | J. Phys. Chem. C 2014, 118, 19505−19523

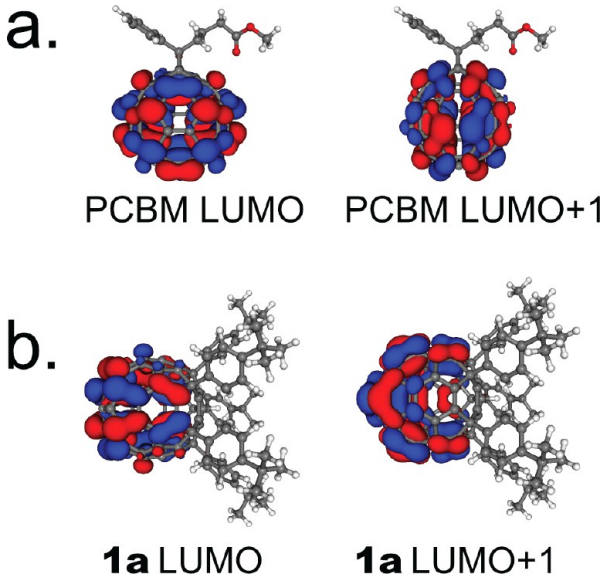

Figure 13. Kohn–Sham orbitals corresponding to the LUMO and LUMO + 1 of (a) PCBM and (b) **1a** calculated using the B3LYP functional and STO-3G basis set.

The results of our calculations thus suggest that there are multiple criteria for choosing a fullerene for best photovoltaic device performance. A good fullerene acceptor must have both a good local mobility (i.e., high probability for electron transfer between nearest neighbors) and a good macroscopic mobility, which depends on the networked formed by the fullerenes on the length scale of the device. To experimentally test whether this idea of both local and global mobility contribute to device performance, we used time-resolved microwave conductivity TRMC[103,104] to measure directly the local conductivity of different fullerenes. Figure 14 shows the photoconductance

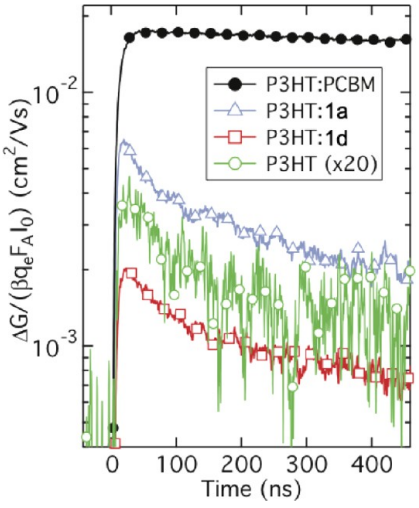

Figure 14. TRMC photoconducance transients of P3HT:SC samples (blue ▲, **1a**; red ■, **1d**) compared with pure P3HT (green ○, multiplied by 20) and P3HT:PCBM (black ●) films. All samples were excited at 500 nm with a pulse fluence of 0.56 mJ/cm^2.

derived from TRMC following photoexcitation of P3HT blend films containing **1a**, **1d**, PCBM, and a P3HT control film with no added fullerene.[95] The P3HT control film shows low photoconductance, indicating that only a few locally mobile holes are generated upon photoexcitation. When either of the two SC molecules is added, the photoconductance increases by a factor of ~20, the result of exciton splitting by the fullerenes. The time profile of the microwave signal does not change, however, indicating that the signal is still dominated by holes on P3HT, so that the local electron mobility on the SC fullerenes is lower than the hole mobility on P3HT. The magnitude of the microwave signal is somewhat larger for the stacking molecule **1a** than the nonstacking **1d**, but the signal depends on the product of the carrier concentration and mobility. In separate time-resolved photoluminescence experiments, we found that there are indeed more carriers produced in P3HT films with **1a** than with **1d** because of the differing degrees of phase separation for these two molecules.[95] The net result is that our TRMC measurements verify our calculations by showing that both SC molecules have similar local mobilities.

Figure 14 also shows that the P3HT:PCBM blend film has a much higher photocondutance than either of the two SC molecules. Since the degree of PL quenching in the PCBM blend is similar to that in the blend with **1a**, this strongly suggests that the local mobility between PCBM molecules is indeed much higher than that between SC molecules, again in accord with our calculations. Moreover, the time profile of this PCBM microwave transient is also different from the other samples, indicating that electron mobility now contributes significant to the signal, so that the local electron mobility on PCBM is comparable to or greater than the local hole mobility on P3HT.

Overall, both the theoretical and experimental results verify that there are indeed two length scales over which mobility must be optimized to produce the best organic photovoltaic devices. Shuttlecock **1a** produces networks that could support excellent macroscopic mobility (as compared to devices based on SC **1d**) but has poor local mobility and thus makes mediocre devices. In contrast, molecules like PCBM have excellent local mobility but make poor macroscopic networks, leading to good device performance that could be further improved if the macroscopic network could be better-controlled. All of these results suggest a simple set of design rules for producing the next generation of fullerene acceptors for polymer-based photovoltaics: the fullerenes must have spherical LUMOs that have strong electronic coupling with their neighbors for good local mobility, but they must also be able to assemble into macroscopic networks that span the device length scale for global mobility. MEEM is currently working on the design and synthesis of new fullerenes that should meet both of these criteria.

3.2.2. Self-Assembling Polymers for Control Over Nanoscale Photovoltaic Morphology. The SCs discussed above demonstrate how self-assembly of the fullerene component of a polymer/fullerene photovoltaic can be used to enhance device performance. It is also possible, however, to use self-assembling conjugated polymers to obtain control over morphology and to enhance hole transport through a device.[96] Amphiphilic assembly, involving molecules that contain both polar/charged and nonpolar regions, is one key type of self-assembly that can generate large driving forces for structural rearrangements. To this end, we have created charged semiconducting polymers that can form cylindrical micelles. Many groups have explored the properties of semiconducting polyelectrolytes for applications ranging from optoelectronic devices[105–107] to biological sensors.[108,109] These materials have been shown to make a variety of architectures,[110–112] but to date, we are aware of none in which the molecular geometry has been optimized to form micelles with the conducting polymer axis running parallel to the micelle axis. We

dx.doi.org/10.1021/jp501047j | J. Phys. Chem. C 2014, 118, 19505–19523

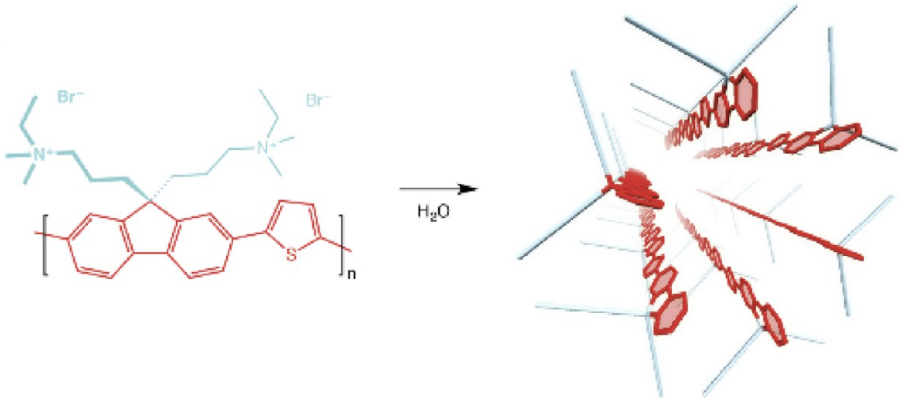

Figure 15. Chemical structure (left) and micellar self-assembly motif (right) of the semiconducting polyelectrolyte PFT.

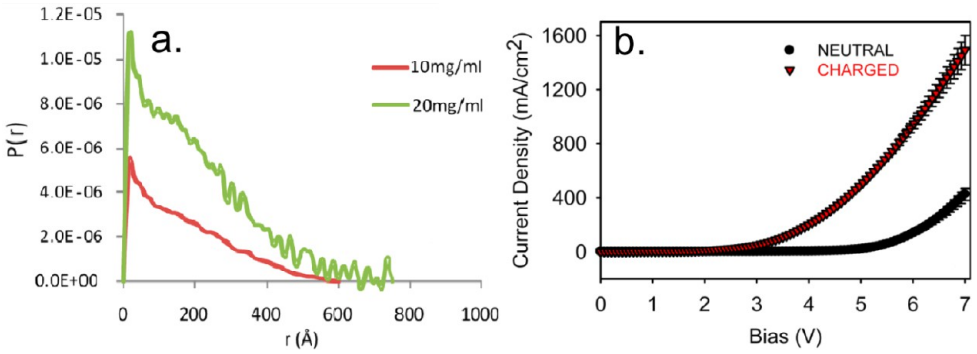

Figure 16. (a) Solution small-angle X-ray scattering (SAXS) probability distribution showing rod-shaped micelles at two different polymer concentrations. (b) Current–voltage characteristics of thin-film diodes of assembled, charged PFT (red ▲), and an unassembled, uncharged PFT analogue (black ●).

have shown in previous work that the best hole conductivity along the polymer occurs along straight, wirelike structure and that kinks and bends can be detrimental to charge transport.[113]

Thus, in our work supported by MEEM, we have extended this idea by using self-assembly to force the polymer chains to couple together into micellar bundles, thus straightening out the polymer backbones because of the geometric constraints associated with forming a micelle. Our first system to achieve this micellar geometry is the amphiphilic semiconducting polymer poly(fluorine-alt thiophene) (PFT), whose chemical structure is shown in Figure 15. PFT has cationic quaternary ammonium side chains and an sp^3-hybridized bridging carbon on each fluorine unit that creates a "pie-wedge"-shaped cross section that allows the polymer to assemble into a cylindrical micelle with the conducting backbone running along the long axis of the cylinder in aqueous solutions. A cartoon of the assembly motif is also shown in Figure 15.

To verify that PFT actually does assemble into cylindrical micelles with straight polymer backbones, we started by using solution-phase small-angle X-ray scattering (SAXS). Figure 16a shows that the probability distribution function, $P(r)$ (obtained as the Fourier transform of the raw X-ray scattering profile) for PFT clearly follows a cylindrical distribution, with a peak corresponding to the micelle diameter and a linear tail that is a clear signature of a rodlike shape.[114] Analysis of the data indicates a micelle diameter of 4 nm, which is consistent with a structure like that in Figure 15 where the micelle is about two molecular diameters across and the π-conjugated planes are arranged radially around the micelle. We also have directly observed that these micelles are preserved when the solutions are cast into the solid state via atomic force microscopy.[96]

In agreement with our initial hypothesis, we find that PFT micelles do indeed show improved conductivity (as demonstrated in Figure 16b), which shows current–voltage curves for diodes fabricated from PFT and a nonquaternized analogue that is soluble in common organic solvents and that does not self-assemble. We find that the self-assembled PFT shows higher currents and lower injection voltages than the same polymer when it is not formed into micelles. Perhaps more importantly, PFT is water-soluble, so that any future devices made from this material can be done with environmentally friendly processing conditions.

As a first step toward producing entirely water-processable organic photovoltaic devices, in ongoing research we have combined PFT with a water-soluble fullerene derivative that is also amphiphilic and contains cationic charges on the fullerene ball.[115,116] The chemical structure of the charged fullerene is shown in the inset to Figure 17. Due to the amphiphilic nature of both PFT and the fullerene, the two species have the ability to coassemble in aqueous solution. We will show in future work that some of these water-soluble fullerenes can coassemble with PFT into micellar architectures. We observe good fluorescence quenching in solution, which proves the fullerenes are in direct contact with the PFT backbone. The existence of a coassembled structure offers the possibility to create a robust network for water-processable photovoltaic devices without the kinetic control inherent in typical BC films. We are already working on second generation polymers and fullerenes with optical properties tuned for a better match to the solar spectrum than is available with PFT.

In addition to the potential benefit for environmentally friendly solar cells, the coassembly of the PFT and the fullerene has also allowed us to tune the photophysics of exciton migration

dx.doi.org/10.1021/jp501047j | J. Phys. Chem. C 2014, 118, 19505–19523

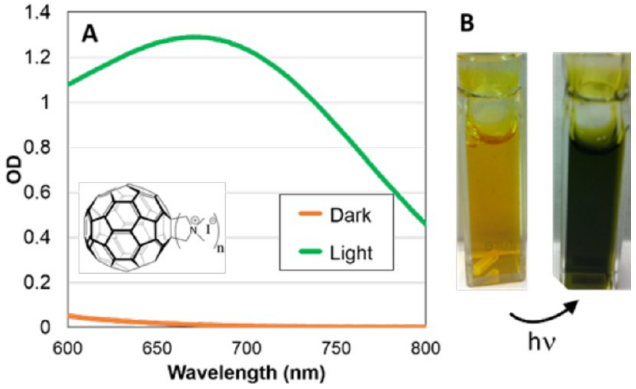

Figure 17. (a) Red portion of the UV−visible absorption spectrum of aqueous solutions of PFT as prepared (orange curve) and after exposure to room light for several minutes (green curve). (b) Photograph of the as-prepared solution (yellow) and the same solution after exposure to room light (dark green).

and charge separation. A prime example of this is the fact that photoexcitation of solutions containing PFT coassembled with charged fullerenes can create long-lived stable polarons in assemblies with optimized structures. Figure 17a shows the UV/vis absorption spectrum of the polymer/fullerene solution as initially prepared and after exposure to visible light. It is clear that exposure to light changes the absorption of the sample, with a new band growing in that is centered near 690 nm. This new band is intense enough that the color change in the sample can be easily observed by eye, and Figure 17b shows that the solution changes from yellow to dark green in color. On the basis of a comparison of the new absorption band to PFT that has been intentionally hole-doped, as well as to the spectrum of the hole polaron in similar conjugated polymers, we assign this new band to the absorption of the PFT hole polaron, created via photoinduced charge transfer to the water-soluble fullerenes that are assembled with the PFT micelle. We also have used ultrafast transient absorption spectroscopy to verify that these polarons, which are stable in solution for weeks, are created on sub-picosecond timescales, consistent with the fluorescence quenching mentioned above. Finally, we will show in future work that varying the substituents on the fullerene derivative can control the placement of the fullerene derivative within the polymer micelle, allowing exquisite tuning of both the forward and back electron transfer rates in this system.

3.3. Using Sequential Processing to Control Organic Photovoltaic Morphology. Whether constructed from self-assembling polymers and fullerenes or more traditional materials, nearly all of the organic photovoltaic devices described in the literature are based on the bulk heterojunction architecture. The introduction of BC films revolutionized the OPV field as it provided the first mechanism to increase the donor/acceptor interfacial area to ensure good exciton harvesting while still allowing interconnected pathways for the carriers to be extracted from the device.[117] As mentioned above, however, the morphology of the two components in a BC film is critical to ensuring good carrier extraction, and this morphology depends not only on the natural degree of mixing/crystallization of the two components but also on the processing kinetics used to make the active layer. This means that slight changes in processing conditions can have strong effects on device performance, making it hard to optimize devices based on new materials[118] or to scale-up devices based on well-studied combinations.

It is for all of these reasons that we have worked to develop an alternate processing method that provides for processing kinetics that are much more reproducible and scalable compared to the traditional BC methods. Our method, referred to as sequential processing (SqP), is based on sequential deposition of the donor and acceptor layers through solvent casting from orthogonal solvents.[97] A typical SqP device might have the polymer layer (e.g., P3HT) cast from a solvent such as *o*-dicholorobenzene (ODCB), followed by casting the fullerene layer (e.g., PCBM) from dichoromethane (DCM). This method works well as long as the polymer underlayer is not soluble in the solvent used to cast the fullerene overlayer, as is indeed the case for P3HT and DCM, particularly if the P3HT powder is extracted in DCM before the ODCB solution is made. In our initial work, we had mistakenly concluded that SqP devices had a bilayer structure,[97] but subsequent work from both our group using TRMC[100] and other groups using neutron reflection[119] and other techniques[120−122] has shown that there is a significant degree of interpenetration of the fullerene from the overlayer into the polymer underlayer. Subsequently, dozens of groups have worked to explore the differences between devices fabricated from BC and SqP methods.[123−131]

The key questions concerning devices built on SqP are how does the fullerene penetrate into the polymer underlayer, and how is the resulting film morphology different/more controllable than that produced by simply preblending the materials in a BC film? Probably the most significant difference between BC and SqP devices comes in the crystallinity of the polymer underlayer. For polymers like P3HT, which tend to crystallize when cast into films, devices built from the BC method have much less crystalline P3HT because the presence of the fullerene inhibits crystallization. As discussed further below, however, casting the fullerene overlayer in SqP devices does not alter the crystallinity of the polymer underlayer.[97] Thus, films produced via SqP can have highly crystalline P3HT, particularly if the polymer underlayer is cast from a slowly evaporating solvent. Since the carrier mobility in P3HT is directly related to the degree of crystallinity, SqP offers better control over the polymer morphology since the polymer crystallinity can be tuned by the choice of casting solvent. Perhaps most importantly, SqP provides for greater reproducibility in producing polymer photovoltaics, particularly when the device area is increased. Figure 18a compares the photovoltaic performance of two sets of small-area (∼7 mm^2) devices with the same active layer thickness and the same molar composition of P3HT and PCBM, one set prepared as a BC film by mixing the components in solution first and the other prepared by SqP. The two sets of devices behave similarly. When the same films are used to make larger-area (∼34 mm^2) devices, however, Figure 18b shows that the SqP devices not only outperform the BC devices but also perform more consistently: the error bars mark ±1 standard deviation in a sampling of over 20 devices of each type. Thus, SqP provides a significant step toward removing the irreproducibility that is inherent in the kinetic control of blend morphology when blend casting devices.

Moreover, SqP also offers the opportunity to alter the polymer underlayer in other ways, such as chemically doping the polymer with agents that would react with the fullerene if present in a bulkheterojunction (BHJ)[128] and rubbing the polymer layer to align polymer chains.[124] Another new use for SqP is as a means to control donor/acceptor vertical phase separation in BHJ films. Several groups have shown that a charge extraction misbalance due to an improper active layer/electrode interface can cause a reduction in the device fill factor, giving an S-shaped current−voltage curve.[132−134] We have argued that S-shaped current−voltage characteristic is caused particularly by a lack of fullerene

dx.doi.org/10.1021/jp501047j | J. Phys. Chem. C 2014, 118, 19505−19523

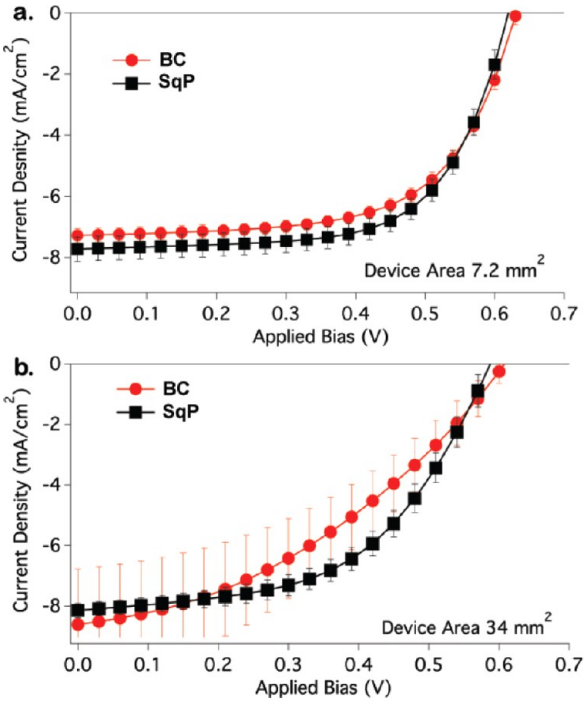

Figure 18. (a) Current−voltage characteristics of two sets of P3HT-PCBM photovoltaic devices, all with the same active layer thickness and identical molar ratios of P3HT and PCBM, with the active layers produced by blend casting (red ●) or via SqP (■). (a) shows the average behavior and standard deviation (error bars) for devices with 7.2 mm^2 area, while (b) shows the same for 34 mm^2 devices.

at the top of a film, the result of processing kinetics that cause the fullerene to "sink" into the polymer while the film is forming, creating a barrier which limits electron extraction at the cathode.[98,135] This vertical phase separation can be put to good use by constructing an "inverted" device, with the cathode on the bottom and the anode deposited on top,[136] or one can remedy the problem directly by sequentially depositing additional fullerene on top of the BHJ, as we have shown.[98] The presence of this additional fullerene corrects the misbalance of charge extraction at the top electrode and removes the S-shaped current−voltage curve, providing another example of the versatility of the SqP technique at controlling OPV morphology.

As has been argued by several groups,[127,129,137−139] including our own,[99,100] when the fullerene is cast on top of a polymer underlayer, the fullerene solvent can swell the amorphous regions of the polymer, allowing the fullerene to enter the amorphous regions of the polymer underlayer without altering its crystallinity. Thus, the fullerene in SqP films is present in a network that follows the contour of the polymer crystallites, and is guaranteed to be connected to the top electrode, providing for a better morphology than is typically obtained in a BC film. To understand what difference the SqP morphology makes in the dynamics of exciton motion and charge separation, we performed a series of ultrafast spectroscopic experiments on BC and SqP films of P3HT and PCBM with the same amount of each material present in both films. Following 530 nm excitation, Figure 19 compares the ultrafast transient absorption dynamics from a film of pure P3HT, a P3HT:PCBM BC, and a P3HT/PCBM SqP film with the same total thickness and total amount of polymer and fullerene as the BHJ film.[99] The broad feature centered at ∼1150 nm is the transient absorption of the P3HT exciton, and in the pure P3HT film (panel a) this absorption

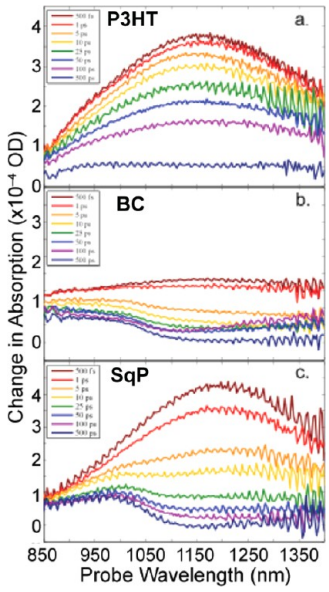

Figure 19. Ultrafast transient absorption of (a) pure P3HT, (b) BC, and (c) SqP P3HT:PCBM films following excitation at 530 nm as a function of time. The P3HT exciton absorption is centered near 1150 nm, while the P3HT polaron band appears at ∼980 nm.

decays on the same timescale as the photoluminescence, as expected. In the BC film (panel b), it is clear that even only 0.5 ps after excitation, over half of the excitons already have been quenched, which gives the results of charge separation on ultrafast timescales.[140] One of the products of the charge separation is a hole polaron on P3HT, which has a broad, weak absorption centered near ∼950 nm that persists on to the nanoseconds timescale. When the same experiment is done on the SqP film, however, the dynamics look completely different: there is initially no exciton quenching, but after a few ps, quenching begins until the same total number of polarons is produced as in the BC film. The fact that the exciton quenching and polaron production dynamics are different is a direct proof that the morphology of BC and SqP films must also be different. We observed that these differences in ultrafast charge separation dynamics persist whether or not there is only a small amount of fullerene present in the film or if the films contain the same amount of fullerene used to produce optimal devices.[99] Thus, SqP films are different from BC films in multiple ways, including the crystallinity of the polymer, the nanometer-scale phase separation of the polymer and the fullerene, and the interconnectedness of the polymer and fullerene networks across the thickness of the film.

4. CONCLUSIONS

A central theme for the experimental studies at MEEM has dealt with the creation of pseudocapacitor materials with appropriate nanoscale architecture. Accordingly, we have emphasized the study of template-directed mesoporous transition metal oxides, in which the interconnected pore network provides electrolyte access to the high surface area, electrochemically active walls, and where sufficiently thick pore walls maintain adequate electronic conductivity for the redox reactions. Our results with Nb_2O_5 mesoporous films indicate not only that Li^+ insertion is extremely rapid but also that this material possesses much better charge storage kinetics than other transition metal oxides. Moreover, the orthorhombic *T*-phase in particular is found to exhibit high specific capacitance at high rate with values of nearly 450 F/g achieved in less than 1 min, far superior to the corresponding

dx.doi.org/10.1021/jp501047j | J. Phys. Chem. C 2014, 118, 19505−19523

state-of-the-art battery materials. We were able to attribute the high level of energy storage at high rates in Nb_2O_5 to an intercalation pseudocapacitance mechanism. Its characteristic electrochemical features include currents that vary inversely with time, charge-storage capacity that is mostly independent of rate and redox peaks that exhibit small voltage offsets, and therefore good reversibility, at high rates. Kinetic studies indicate that for charging times of 1 min or longer, there are no indications of ionic diffusion limitations and the current response is capacitor-like. First-principle density-functional calculations and multiscale modeling have been directed at developing physical models and accurate numerical tools to describe ion intercalation into the electrode material, processes at electrode/electrolyte interface, and the relation between the electrochemical properties and electrode morphology.

MEEM has focused on improving OPV device morphology through two main fronts, self-assembly and sequential processing. We have shown that self-assembly can be used to control the structure within a solar cell active layer. Self-assembly has been shown to increase current extraction within both the donor and acceptor network. We have also explored sequential processing as an alternative to the traditional bled cast fabrication method. Our studies show that SqP and BC films differ in structure and charge generation. SqP also opens prospect of manipulating the polymer film prior to fullerene deposition. Furthermore, we were able to eliminate detrimental s-shaped current voltage curves by depositing additional fullerene onto a BHJ film. We hope to apply what we have learned to the next generation of organic photovoltaic materials to making reproducible, large-scale, high-efficiency photovoltaics.

AUTHOR INFORMATION

Corresponding Authors

*E-mail: schwartz@chem.ucla.edu.
*E-mail: bdunn@ucla.edu.
*E-mail: vidvuds@ucla.edu.

Notes

The authors declare no competing financial interest.

Biographies

Jordan C. Aguirre received a Bachelors of Science in chemistry in 2009 from the University of California Los Angeles (UCLA). He is currently pursuing a Ph.D. in physical chemistry from UCLA in the department of Chemistry and Biochemistry. He has previously worked as a summer intern at the National Renewable Energy Laboratory in the National Center for Photovoltaics. Jordan enjoys volunteering his time to generate interest in science by teaching experiments to high school teachers for the California NanoSystems Institute (CNSI) high school nanoscience program.

Amy S. Ferreira attended the University of California, Riverside (UCR) where she received her Bachelors of Science in chemistry in 2009. While there, she worked under Prof. Valentine Vullev on the study of charge transfer rates through amide bonds. She is currently pursuing a Ph.D. in physical chemistry at UCLA under the supervision of Prof. Sarah Tolbert. Amy currently works on characterizing organic photovoltaics and is also a Clean Green IGERT fellow.

Hong "Kevin" Ding received his Bachelor's degree in Materials Science and Engineering (2010) from Shanghai Jiaotong University in China. He is currently a Ph.D. student in the group of Prof. Mark Asta at UC Berkeley. The principal focus of his research is to understand the thermodynamic, kinetic, and mechanical properties of a wide range of technological important materials with computational materials science methods.

Samson A. Jenekhe holds the Boeing-Martin Endowed Professor of Chemical Engineering and Professor of Chemistry at the University of Washington, which he assumed in 2000. He graduated from Michigan Technological University with a B.S. degree in 1977. His graduate studies were at the University of Minnesota where he received a M.S. (Chemical Engineering, 1980), M.A. (Philosophy, 1981), and Ph.D. (Chemical Engineering, 1985). Following appointments at Honeywell, Inc., Physical Sciences Center, Minneapolis, MN, he started his academic career at the University of Rochester, where he held the positions of Assistant, Associate, and Full Professor of Chemical Engineering, Professor of Materials Science, and Professor of Chemistry during 1988-2000. His research interests are in the chemistry, physics, and engineering applications of polymer semiconductors, organic electronic and optoelectronic devices, materials and devices for solar energy technologies, self-assembly and soft nanotechnology, and polymer science.

Nikos Kopidakis is a Senior Research Scientist at the Chemical and Materials Science Center of the National Renewable Energy Laboratory. His research focuses on using photoconductivity techniques to study solar cell materials. He is interested in the fundamental photophysical processes in organic semiconductors and also in the development of next generation materials and device architectures for solar energy conversion.

Mark Asta is Professor and Chair in the Department of Materials Science and Engineering at UC Berkeley, where he received his Ph.D. in 1993. Prior to joining the faculty at Berkeley he was a staff member at Sandia National Laboratories, a faculty member at Northwestern University, and then a faculty member at UC Davis. His research focuses on the application of first-principles density-functional-theory and classical atomistic simulations to the study of the structure and properties of materials for advanced structural and energy applications.

Laurent Pilon received his Ph.D. from Purdue University in 2002. He then joined the Mechanical and Aerospace Engineering Department at UCLA where he is now Full Professor. His research group is engaged in a wide range of interdisciplinary research projects at the intersection between interfacial and transport phenomena, material science, and biology for sustainable energy conversion, storage, and efficiency technologies.

Yves Rubin received his diploma in chemistry in 1987 from the University of Fribourg in Switzerland with Professors Albert Gossauer and Alexander von Zelewski as diploma thesis advisors. He received his Ph.D. degree at UCLA in 1991 under the guidance of Professor Franois Diederich. From 1991 to 1992, he was a postdoctoral fellow with Professor Ronald Breslow at Columbia University. In 1992, he was appointed as an assistant professor of organic chemistry at UCLA and is a full professor there since 2001. He is the recipient of an Alfred P. Sloan Research Fellowship (1998), the Ruzicka Prize, the National Prize for a Young Swiss Chemist (1997), an NSF Young Investigator Award, an Arnold and Mabel Beckman Young Investigator Award, and a Camille and Henry Dreyfus New Faculty Award.

Sarah H. Tolbert is a Professor in the Departments of Chemistry and Biochemistry and Materials Science and Engineering at UCLA. Prior to joining the faculty at UCLA, she received a B.S. from Yale University, a Ph.D. from UC Berkeley, and was an NSF postdoctoral fellow at UC Santa Barbara. Her research focuses on controlling nanometer-scale architecture in solution-processed nanomaterials to generate unique optical, electronic, magnetic, structural, and electrochemical properties. Her group specifically focuses on solar energy harvesting, electrochemical energy storage, nanomagnetics, and new ultrahard materials. She also leads a program aimed at bringing nanoconcepts to high school students in the greater LA area. Professor Tolbert is the recipient of a

number of awards including the Office of Naval Research Young Investigator Award, an NSF CAREER Award, a Beckman Young Investigator Award, and a Sloan Foundation Research Fellowship.

Benjamin J. Schwartz received his Ph.D. in Experimental Physical Chemistry from UC Berkeley in 1992. After carrying out postdoctoral work in theoretical physical chemistry at the University of Texas, Austin (1993−1995 with Prof. Peter Rossky), and in the spectroscopy and device physics of semiconducting polymers at UC Santa Barbara (1995−1996, with 2000 Nobel Laureate Alan Heeger), he joined the faculty at UCLA in 1997, where he was promoted to Associate Professor with tenure in 2002 and Full Professor in 2004. He has published over 140 papers in peer-reviewed journals and holds 2 U.S. patents with an additional patent pending. Prof. Schwartz has received Teacher-Scholar awards from both the Dreyfus Foundation and the Research Corporation, is a Sloan Foundation Fellow, and is a winner of UCLA's distinguished teaching award. Prof. Schwartz continues to serve as Senior Editor for the Journal of Physical Chemistry, a position he has held for the past 8 years. Prof. Schwartz' current research interests include quantum nonadiabatic processes in condensed phases studied from both theoretical and ultrafast spectroscopic points of view, as well as studies of the fundamental processes underlying the operation of conjugated polymer-based solar cells.

Bruce Dunn is the Nippon Sheet Glass Professor of Materials Science and Engineering at UCLA. Prior to joining UCLA in 1981, he was a staff scientist at the General Electric Research Laboratory. His research interests are in the synthesis of inorganic and organic/inorganic materials, and the design of their electrochemical, optical, and biochemical properties. His current programs in electrochemistry include creating pseudocapacitive materials and the fabrication of three-dimensional batteries. Professor Dunn has received a number of honors, including a Fulbright research fellowship, invited professorships at the University of Paris, the University of Bordeaux, and two awards from the Department of Energy for Outstanding Research in Materials Science. He is a Fellow of the American Ceramic Society and the Materials Research Society.

Vidvuds Ozoliņš is Professor in the Department of Materials Science and Engineering at UCLA. Prior to joining UCLA in 2002, he earned a Ph.D. in Theoretical Physics from the Royal Institute of Technology in Sweden in 1998, was a postdoctoral fellow at the National Renewable Energy Laboratory, and a staff member at Sandia National Laboratories in Livermore, California. His research focuses on first-principles studies of materials for energy storage, generation, and conversion as well as on development of information science based methods for first-principles computational materials science.

■ ACKNOWLEDGMENTS

This work was supported as part of the Molecularly Engineered Energy Materials, an Energy Frontier Research Center funded by the U.S. Department of Energy, Office of Science, Basic Energy Sciences under Award Number DE-SC0001342.

■ REFERENCES

(1) Miller, J.; Burke, A. Electrochemical Capacitors: Challenges and Opportunities for Real-World Applications. *Interface* **2008**, *17*, 53−57.
(2) *Basic Research Needs for Electrical Energy Storage*; Report of the Basic Energy Science Workshop on Electrical Energy Storage, April 2−4, 2007, Office of Basic Energy Sciences, Department of Energy: Washington, D.C., 2007.
(3) Naoi, K.; Simon, P. New Materials and New Configurations for Advanced Electrochemical Capacitors. *Interface* **2008**, *17*, 34−37.
(4) Conway, B. E.; Pell, W. G. Double-Layer and Pseudocapacitance Types of Electrochemical Capacitors and Their Applications to the Development of Hybrid Devices. *J. Solid State Electrochem.* **2003**, *7*, 637−644.
(5) Pandolfo, A. G.; Hollenkamp, A. F. Carbon Properties and Their Role in Supercapacitors. *J. Power Sources* **2006**, *157*, 11−27.
(6) Frackowiak, E. Carbon Materials for Cupercapacitor Application. *Phys. Chem. Chem. Phys.* **2007**, *9*, 1774−1785.
(7) Conway, B. *Electrochemical Supercapacitors: Scientific Fundamentals and Technological Applications*; Kluwer Academic: New York, 1999.
(8) Kim, I. H.; Kim, J. H.; Cho, B. W.; Kim, K. B. Pseudocapacitive Properties of Electrochemically Prepared Vanadium Oxide on Carbon Nanotube Film Substrate. *J. Electrochem. Soc.* **2006**, *153*, A1451−A1458.
(9) Nam, K. W.; Lee, E. S.; Kim, J. H.; Lee, Y. H.; Kim, K. B. Synthesis and Electrochemical Investigations of $Ni_{1-x}O$ Thin Films and $Ni_{1-x}O$ on Three-Dimensional Carbon Substrates for Electrochemical Capacitors. *J. Electrochem. Soc.* **2005**, *152*, A2123−A2129.
(10) Toupin, M.; Brousse, T.; Belanger, D. Charge Storage Mechanism of Mno_2 Electrode Used in Aqueous Electrochemical Capacitor. *Chem. Mater.* **2004**, *16*, 3184−3190.
(11) Cottineau, T.; Toupin, M.; Delahaye, T.; Brousse, T.; Belanger, D. Nanostructured Transition Metal Oxides for Aqueous Hybrid Electrochemical Supercapacitors. *Appl. Phys. A: Mater. Sci. Process.* **2006**, *82*, 599−606.
(12) Brezesinski, T.; Wang, J.; Polleux, J.; Dunn, B.; Tolbert, S. H. Templated Nanocrystal-Based Porous TiO_2 Films for Next-Generation Electrochemical Capacitors. *J. Am. Chem. Soc.* **2009**, *131*, 1802−1809.
(13) Brezesinski, K.; Wang, J.; Haetge, J.; Reitz, C.; Steinmueller, S. O.; Tolbert, S. H.; Smarsly, B. M.; Dunn, B.; Brezesinski, T. Pseudocapacitive Contributions to Charge Storage in Highly Ordered Mesoporous Group V Transition Metal Oxides with Iso-Oriented Layered Nanocrystalline Domains. *J. Am. Chem. Soc.* **2010**, *132*, 6982−6990.
(14) Brezesinski, T.; Wang, J.; Senter, R.; Brezesinski, K.; Dunn, B.; Tolbert, S. H. On the Correlation between Mechanical Flexibility, Nanoscale Structure, and Charge Storage in Periodic Mesoporous CeO_2 Thin Films. *ACS Nano* **2010**, *4*, 967−977.
(15) Brezesinski, T.; Wang, J.; Tolbert, S. H.; Dunn, B. Ordered Mesoporous α-MoO_3 with Iso-Oriented Nanocrystalline Walls for Thin-Film Pseudocapacitors. *Nat. Mater.* **2010**, *9*, 146−151.
(16) Reichman, B.; Bard, A. J. Electrochromism at Niobium Pentoxide Electrodes in Aqueous and Acetonitrile Solutions. *J. Electrochem. Soc.* **1980**, *127*, 241−242.
(17) Kodama, R.; Terada, Y.; Nakai, I.; Komaba, S.; Kumagai, N. Electrochemical and In Situ XAFS-XRD Investigation of Nb_2O_5 for Rechargeable Lithium Batteries. *J. Electrochem. Soc.* **2006**, *153*, A583−A588.
(18) Kim, J. W.; Augustyn, V.; Dunn, B. The Effect of Crystallinity on the Rapid Pseudocapacitive Response of Nb_2O_5. *Adv. Energy Mater.* **2012**, *2*, 141−148.
(19) Ardizzone, S.; Fregonara, G.; Trasatti, S. Inner and Outer Active Surface of RuO_2 Electrodes. *Electrochim. Acta* **1990**, *35*, 263−267.
(20) Augustyn, V.; Come, J.; Lowe, M. A.; Kim, J. W.; Taberna, P.-L.; Tolbert, S. H.; Abrua, H. D.; Simon, P.; Dunn, B. High-Rate Electrochemical Energy Storage Through Li^+ Intercalation Pseudocapacitance. *Nat. Mater.* **2013**, *12*, 518−522.
(21) Rauda, I. E.; Augustyn, V.; Dunn, B.; Tolbert, S. H. Enhancing Pseudocapacitive Charge Storage in Polymer Templated Mesoporous Materials. *Acc. Chem. Res.* **2013**, *46*, 1113−1124.
(22) Kresge, C. T.; Leonowicz, M. E.; Roth, W. J.; Vartuli, J. C.; Beck, J. S. Ordered Mesoporous Molecular-Sieves Synthesized by a Liquid-Crystal Template Mechanism. *Nature* **1992**, *359*, 710−712.
(23) Zhao, D.; Feng, J.; Huo, Q.; Melosh, N.; Fredrickson, G. H.; Chmelka, B. F.; Stucky, G. D. Triblock Copolymer Syntheses of Mesoporous Silica with Periodic 50 to 300 Angstrom Pores. *Science* **1998**, *279*, 548−552.
(24) Templin, M.; Franck, A.; DuChesne, A.; Leist, H.; Zhang, Y. M.; Ulrich, R.; Schadler, V.; Wiesner, U. Organically Modified Aluminosilicate Mesostructures from Block Copolymer Phases. *Science* **1997**, *278*, 1795−1798.

(25) Lu, Y. F.; Ganguli, R.; Drewien, C. A.; Anderson, M. T.; Brinker, C. J.; Gong, W. L.; Guo, Y. X.; Soyez, H.; Dunn, B.; Huang, M. H.; et al. Continuous Formation of Supported Cubic and Hexagonal Mesoporous Films by Sol Gel Dip-Coating. *Nature* **1997**, *389*, 364−368.
(26) Rauda, I. E.; Buonsanti, R.; Saldarriaga-Lopez, L. C.; Benjauthrit, K.; Schelhas, L. T.; Stefik, M.; Augustyn, V.; Ko, J.; Dunn, B.; Wiesner, U.; et al. General Method for the Synthesis of Hierarchical Nanocrystal-Based Mesoporous Materials. *ACS Nano* **2012**, *6*, 6386−6399.
(27) Rauda, I. E.; Saldarriaga-Lopez, L. C.; Helms, B. A.; Schelhas, L. T.; Membreno, D.; Milliron, D. J.; Tolbert, S. H. Nanoporous Semiconductors Synthesized Through Polymer Templating of Ligand-Stripped CdSe Nanocrystals. *Adv. Mater.* **2013**, *25*, 1315−1322.
(28) Warren, S. C.; Messina, L. C.; Slaughter, L. S.; Kamperman, M.; Zhou, Q.; Gruner, S. M.; DiSalvo, F. J.; Wiesner, U. Ordered Mesoporous Materials from Metal Nanoparticle-Block Copolymer Self-Assembly. *Science* **2008**, *320*, 1748−1752.
(29) Deshpande, A. S.; Pinna, N.; Smarsly, B.; Antonietti, M.; Niederberger, M. Controlled Assembly of Preformed Ceria Nanocrystals into Highly Ordered 3D Nanostructures. *Small* **2005**, *1*, 313−316.
(30) Ba, J. H.; Polleux, J.; Antonietti, M.; Niederberger, M. Non-Aqueous Synthesis of Tin Oxide Nanocrystals and Their Assembly Into Ordered Porous Mesostructures. *Adv. Mater.* **2005**, *17*, 2509−2512.
(31) Dong, A. G.; Ye, X. C.; Chen, J.; Kang, Y. J.; Gordon, T.; Kikkawa, J. M.; Murray, C. B. A Generalized Ligand-Exchange Strategy Enabling Sequential Surface Functionalization of Colloidal Nanocrystals. *J. Am. Chem. Soc.* **2011**, *133*, 998−1006.
(32) Buonsanti, R.; Pick, T. E.; Krins, N.; Richardson, T. J.; Helms, B. A.; Milliron, D. J. Assembly of Ligand-Stripped Nanocrystals into Precisely Controlled Mesoporous Architectures. *Nano Lett.* **2012**, *12*, 3872−3877.
(33) Rivest, J. B.; Buonsanti, R.; Pick, T. E.; Zhu, L. N.; Lim, E.; Clavero, C.; Schaible, E.; Helms, B. A.; Milliron, D. J. Evolution of Ordered Metal Chalcogenide Architectures through Chemical Transformations. *J. Am. Chem. Soc.* **2013**, *135*, 7446−7449.
(34) Zou, D.; Ma, S.; Guan, R.; Park, M.; Sun, L.; Aklonis, J. J.; Salovey, R. Model Filled Polymers. V. Synthesis of Crosslinked Monodisperse Polymethacrylate Beads. *J. Polym. Sci., Part A: Polym. Chem.* **1992**, *30*, 137−144.
(35) Wang, T. W.; Sel, O.; Djerdj, I.; Smarsly, B. Preparation of a Large Mesoporous CeO_2 with Crystalline Walls Using PMMA Colloidal Crystal Templates. *Colloid Polym. Sci.* **2006**, *285*, 1−9.
(36) Graeber, E. J.; Morosin, B. The Molecular Configuration of the Decaniobate Ion $(Nb_{17}O_{28})^{6-}$. *Acta Crystallogr., Sect. B* **1977**, *33*, 2137−2143.
(37) Villa, E. M.; Ohlin, C. A.; Balogh, E.; Anderson, T. M.; Nyman, M. D.; Casey, W. H. Reaction Dynamics of the Decaniobate Ion $[H_xNb_{10}O_{28}]^{(6-X)-}$ in Water. *Angew. Chem., Int. Ed.* **2008**, *47*, 4844−4846.
(38) McKeown, D. A.; Hagans, P. L.; Carette, L. P. L.; Russell, A. E.; Swider, K. E.; Rolison, D. R. Structure of Hydrous Ruthenium Oxides: Implications for Charge Storage. *J. Phys. Chem. B* **1999**, *103*, 4825−4832.
(39) Sugimoto, W.; Yokoshima, K.; Murakami, Y.; Takasu, Y. Charge Storage Mechanism of Nanostructured Anhydrous and Hydrous Ruthenium-Based Oxides. *Electrochim. Acta* **2006**, *52*, 1742−1748.
(40) Rolison, D. R.; Long, J. W.; Lytle, J. C.; Fischer, A. E.; Rhodes, C. P.; McEvoy, T. M.; Bourg, M. E.; Lubers, A. M. Multifunctional 3D Nanoarchitectures for Energy Storage and Conversion. *Chem. Soc. Rev.* **2009**, *38*, 226−252.
(41) Over, H. Surface Chemistry of Ruthenium Dioxide in Heterogeneous Catalysis and Electrocatalysis: From Fundamental to Applied Research. *Chem. Rev.* **2012**, *112*, 3356−3426.
(42) Sorantin, P. I.; Schwarz, K. Chemical Bonding in Rutile-Type Compounds. *Inorg. Chem.* **1992**, *31*, 567−576.
(43) Trasatti, S.; Buzzanca, G. Ruthenium Dioxide: A New Interesting Electrode Material. Solid State Structure and Electrochemical Behaviour. *J. Electroanal. Chem.* **1971**, *29*, A1−A5.
(44) Liu, Y.; Zhou, F.; Ozoliņš, V. Ab Initio Study of the Charge-Storage Mechanisms in RuO_2-Based Electrochemical Ultracapacitors. *J. Phys. Chem. C* **2012**, *116*, 1450−1457.
(45) Ozoliņš, V.; Zhou, F.; Asta, M. Ruthenia-Based Electrochemical Supercapacitors: Insights from First-Principles Calculations. *Acc. Chem. Res.* **2013**, *46*, 1084−1093.
(46) Zheng, J. P.; Cygan, P. J.; Jow, T. R. Hydrous Ruthenium Oxide as an Electrode Material for Electrochemical Capacitors. *J. Electrochem. Soc.* **1995**, *142*, 2699−2703.
(47) Dmowski, W.; Egami, T.; Swider-Lyons, K. E.; Love, C. T.; Rolison, D. R. Local Atomic Structure and Conduction Mechanism of Nanocrystalline Hydrous RuO_2 from X-ray Scattering. *J. Phys. Chem. B* **2002**, *106*, 12677−12683.
(48) Majzoub, E. H.; Ozoliņš, V. Prototype Electrostatic Ground State Approach to Predicting Crystal Structures of Ionic Compounds: Application to Hydrogen Storage Materials. *Phys. Rev. B* **2008**, *77*, 104115.
(49) Majzoub, E. H.; Zhou, F.; Ozolinš, V. First-Principles Calculated Phase Diagram for Nanoclusters in the Na-Al-H System: A Single-Step Decomposition Pathway for $NaAlH_4$. *J. Phys. Chem. C* **2011**, *115*, 2636−2643.
(50) Sugimoto, W.; Iwata, H.; Yokoshima, K.; Murakami, Y.; Takasu, Y. Proton and Electron Conductivity in Hydrous Ruthenium Oxides Evaluated by Electrochemical Impedance Spectroscopy: The Origin of Large Capacitance. *J. Phys. Chem. B* **2005**, *109*, 7330−7338.
(51) Hu, C.-C.; Chang, K.-H.; Lin, M.-C.; Wu, Y.-T. Design and Tailoring of the Nanotubular Arrayed Architecture of Hydrous RuO_2 for Next Generation Supercapacitors. *Nano Lett.* **2006**, *6*, 2690−2695.
(52) Lin, K.-M.; Chang, K.-H.; Hu, C.-C.; Li, Y.-Y. Mesoporous RuO_2 for the Next Generation Supercapacitors with an Ultrahigh Power Density. *Electrochim. Acta* **2009**, *54*, 4574−4581.
(53) Sitepu, H. Texture and Structural Refinement Using Neutron Diffraction Data From Molybdite (MoO_3) and Calcite $(CaCO_3)$ Powders and a Ni-Rich $Ni_{50.7}Ti$)49.30 Alloy. *Powder Diffr.* **2009**, *24*, 315−326.
(54) Negishi, H.; Negishi, S.; Kuroiwa, Y.; Sato, N.; Aoyagi, S. Anisotropic Thermal Expansion of Layered MoO_3 Crystals. *Phys. Rev. B* **2004**, *69*, 064111.
(55) Grimme, S. Semiempirical GGA-Type Density Functional Constructed with a Long-Range Dispersion Correction. *J. Comput. Chem.* **2006**, *27*, 1787−1799.
(56) Klimeš, J.; Bowler, D. R.; Michaelides, A. Chemical Accuracy for the van der Waals Density Functional. *J. Phys.: Condens. Matter* **2010**, *22*, 022201.
(57) Dudarev, S. L.; Botton, G. A.; Savrasov, S. Y.; Humphreys, C. J.; Sutton, A. P. Electron-Energy-Loss Spectra and the Structural Stability of Nickel Oxide: An LSDA+*U* Study. *Phys. Rev. B* **1998**, *57*, 1505−1509.
(58) Berthumeyrie, S.; Badot, J. C.; Pereira-Ramos, J. P.; Dubrunfaut, O.; Bach, S.; Vermaut, P. Influence of Lithium Insertion on the Electronic Transport in Electroactive MoO_3 Nanobelts and Classical Powders: Morphological and Particle Size Effects. *J. Phys. Chem. C* **2010**, *114*, 19803−19814.
(59) Julien, C.; Khelfa, A.; Hussain, O. M.; Nazri, G. A. Synthesis and Characterization of Flash-Evaporated MoO_3 Thin Films. *J. Cryst. Growth* **1995**, *156*, 235−244.
(60) Hong, D.; Lin, H.; Sadigh, B.; Zhou, F.; Ozoliņš, V.; Asta, M. Computational Investigation of Electron Small Polarons in α-MoO_3. *J. Phys. Chem. C* **2014**, in press, 10.1021/jp503065x.
(61) Wang, H. N.; Pilon, L. Accurate Simulations of Electric Double Layer Capacitance of Ultramicroelectrodes. *J. Phys. Chem. C* **2011**, *115*, 16711−16719.
(62) Booth, F. The Dielectric Constant of Water and the Saturation Effect. *J. Chem. Phys.* **1951**, *19*, 391−394.
(63) Booth, F. Dielectric Constant of Polar Liquids at High Field Strengths. *J. Chem. Phys.* **1955**, *23*, 453−457.
(64) Yang, L.; Fishbine, B. H.; Migliori, A.; Pratt, L. R. Dielectric Saturation of Liquid Propylene Carbonate in Electrical Energy Storage Applications. *J. Chem. Phys.* **2010**, *132*, 044701.

(65) Outhwaite, C. W.; Bhuiyan, L. B. An Improved Modified Poisson-Boltzmann Equation in Electric-Double-Layer Theory. *J. Chem. Soc., Faraday Trans. 2* **1983**, *79*, 707−718.
(66) Bazant, M. Z.; Kilic, M. S.; Storey, B. D.; Ajdari, A. Towards an Understanding of Induced-Charge Electrokinetics at Large Applied Voltages in Concentrated Solutions. *Adv. Colloid Interface Sci.* **2009**, *152*, 48−88.
(67) Wang, H. N.; Pilon, L. Mesoscale Modeling of Electric Double Layer Capacitors with Three-Dimensional Ordered Structures. *J. Power Sources* **2013**, *221*, 252−260.
(68) Woo, S. W.; Dokko, K.; Nakano, H.; Kanamura, K. Preparation of Three Dimensionally Ordered Macroporous Carbon with Mesoporous Walls for Electric Double-Layer Capacitors. *J. Mater. Chem.* **2008**, *18*, 1674−1680.
(69) Wang, H.; Fang, J.; Pilon, L. Scaling Laws for Carbon-Based Electric Double Layer Capacitors. *Electrochim. Acta* **2013**, *109*, 316−321.
(70) Kilic, M. S.; Bazant, M. Z.; Ajdari, A. Steric Effects in the Dynamics of Electrolytes at Large Applied Voltages. II. Modified Poisson-Nernst-Planck Equations. *Phys. Rev. E* **2007**, *75*, 021503.
(71) Wang, H. N.; Pilon, L. Physical Interpretation of Cyclic Voltammetry for Measuring Electric Double Layer Capacitances. *Electrochim. Acta* **2012**, *64*, 130−139.
(72) Wang, H. N.; Pilon, L. Intrinsic limitations of Impedance Measurements in Determining Electric Double Layer Capacitances. *Electrochim. Acta* **2012**, *63*, 55−63.
(73) Wang, H. N.; Pilon, L. Reply to Comments on "Intrinsic limitations of Impedance Measurements in Determining Electric Double Layer Capacitances" by H. Wang and L. Pilon [Electrochim. Acta **2012**, *63*, 55]. *Electrochim. Acta* **2012**, *76*, 529−531.
(74) d'Entremont, A.; Pilon, L. First-Principles Thermal Modeling of Electric Double Layer Capacitors Under Constant-Current Cycling. *J. Power Sources* **2014**, *246*, 887−898.
(75) Wang, H.; Thiele, A.; Pilon, L. Simulations of Cyclic Voltammetry for Electric Double Layers in Asymmetric Electrolytes: A Generalized Modified Poisson-Nernst-Planck Model. *J. Phys. Chem. C* **2013**, *117*, 18286−18297.
(76) Green, M. A.; Emery, K.; Hishikawa, Y.; Warta, W.; Dunlop, E. D. Solar Cell Efficiency Tables (Version 42). *Progress in Photovolaics Research and Application* **2013**, *21*, 827−837.
(77) van Bavel, S. S.; Sourty, E.; With, G. d.; Loos, J. Three-Dimensional Nanoscale Organization of Bulk Heterojunction Polymer Solar Cells. *Nano Lett.* **2009**, *9*, 507−513.
(78) Halls, J. J. M.; Walsh, C. A.; Greenham, N.; Marseglia, E. A.; Friend, R.; Moratti, S. C.; Holmes, A. Efficient Photodiodes from Interpenetrating Polymer Networks. *Nature* **1995**, *376*, 498−500.
(79) Shaheen, S. E.; Brabec, C. J.; Sariciftci, N. S.; Padinger, F.; Fromherz, T.; Hummelen, J. C. 2.5% Efficient Organic Plastic Solar Cells. *Appl. Phys. Lett.* **2001**, *78*, 841−843.
(80) Ma, W.; Yang, C.; Gong, X.; Lee, K.; Heeger, A. Thermally Stable, Efficient Polymer Solar Cells with Nanoscale Control of the Interpenetrating Network Morphology. *Adv. Funct. Mater.* **2005**, *15*, 1617−1622.
(81) Kim, K.; Liu, J.; Namboothiry, M. A. G.; Carroll, D. L. Roles of Donor and Acceptor Nanodomains in 6% Efficient Thermally Annealed Polymer Photovoltaics. *Appl. Phys. Lett.* **2007**, *90*, 163511.
(82) Verploegen, E.; Mondal, R.; Bettinger, C. J.; Sok, S.; Toney, M. F.; Bao, Z. Effects of Thermal Annealing Upon the Morphology of Polymer/Fullerene Blends. *Adv. Funct. Mater.* **2010**, *20*, 3519−3529.
(83) Li, G.; Shrotriya, V.; Huang, J.; Yao, Y.; Moriarty, T.; Emery, K.; Yang, Y. High-Efficiency Solution Processable Polymer Photovoltaic Cells by Self-Organization of Polymer Blends. *Nat. Mater.* **2005**, *4*, 864−868.
(84) Kim, Y.; Choulis, S. A.; Nelson, J.; Bradley, D. D. C.; Cook, S.; Durrant, J. R. Device Annealing Effect in Organic Solar Cells with Blends of Regioregular Poly(3-Hexylthiophene) and Soluble Fullerene. *Appl. Phys. Lett.* **2005**, *86*, 063502.
(85) Vanlaeke, P.; Vanhoyland, G.; Aernouts, T.; Cheyns, D.; Deibel, C.; Manca, J.; Heremans, P.; Poortmans, J. Polythiophene Based Bulk Heterojunction Solar Cells: Morphology and Its Implications. *Thin Solid Films* **2006**, *511*−*512*, 358−361.
(86) Zhao, Y.; Xie, Z.; Qu, Y.; Geng, Y.; Wang, L. Solvent-Vapor Treatment Induced Performance Enhancement of Poly(3-Hexylthiophene): Methanofullerene Bulk-Heterojunction Photovoltaic Cells. *Appl. Phys. Lett.* **2007**, *90*, 043504.
(87) Jo, J.; Na, S.-I.; Kim, S.-S.; Lee, T.-W.; Chung, Y.; Kang, S.-J.; Vak, D.; Kim, D.-Y. Three-Dimensional Bulk Heterojunction Morphology for Achieving High Internal Quantum Efficiency in Polymer Solar Cells. *Adv. Funct. Mater.* **2009**, 2398−2406.
(88) Peet, J.; Soci, C.; Coffin, R. C.; Nguyen, T. Q.; Mikhailovsky, A.; Moses, D.; Bazan, G. C. Method for Increasing the Photoconductive Response in Conjugated Polymer/Fullerene Composites. *Appl. Phys. Lett.* **2006**, *89*, 252105.
(89) Peet, J.; Kim, J. Y.; Coates, N. E.; Ma, W. L.; Moses, D.; Heeger, A. J.; Bazan, G. C. Efficiency Enhancement in Low-Bandgap Polymer Solar Cells by Processing with Alkane Dithiols. *Nat. Mater.* **2007**, *6*, 497−500.
(90) Lee, J. K.; Ma, W. L.; Brabec, C. J.; Yuen, J.; Moon, J. S.; Kim, J. Y.; Lee, K.; Bazan, G. C.; Heeger, A. J. Processing Additives for Improved Efficiency from Bulk Heterojunction Solar Cells. *J. Am. Chem. Soc.* **2008**, *130*, 3619−3623.
(91) Jorgensen, M.; Carlé, J. E.; Søndergaard, R. R.; Lauritzen, M.; Dagnæs-Hansen, N. A.; Byskov, S. L.; Andersen, T. R.; Larsen-Olsen, T. T.; Böttiger, A. P. L.; Andreasen, B.; et al. The State of Organic Solar Cells−A Meta Analysis. *Sol. Energy Mater. Sol. Cells* **2013**, *119*, 84−93.
(92) Kennedy, R. D.; Ayzner, A. L.; Wanger, D. D.; Day, C. T.; Halim, M.; Khan, S. I.; Tolbert, S. H.; Schwartz, B. J.; Rubin, Y. Self-Assembling Fullerenes for Improved Bulk-Heterojunction Photovoltaic Devices. *J. Am. Chem. Soc.* **2008**, *130*, 17290−17292.
(93) Tassone, C. J.; Ayzner, A. L.; Kennedy, R. D.; Halim, M.; So, M.; Rubin, Y.; Tolbert, S. H.; Schwartz, B. J. Using Pentaarylfullerenes to Understand Network Formation in Conjugated Polymer-Based Bulk-Heterojunction Solar Cells. *J. Phys. Chem. C* **2011**, *115*, 22563−22571.
(94) Kennedy, R. D.; Halim, M.; Khan, S. I.; Schwartz, B. J.; Tolbert, S. H.; Rubin, Y. Crystal-Packing Trends for a Series of 6,9,12,15,18-Pentaaryl-1-Hydro[60]Fullerenes. *Chem.−Eur. J.* **2012**, *18*, 7418−7433.
(95) Aguirre, J. C.; Arntsen, C.; Hernandez, S.; Huber, R.; Nardes, A. M.; Halim, M.; Kilbride, D.; Kopidakis, N.; Tolbert, S. H.; Schwartz, B. J.; et al. Understanding Local and Macroscopic Electron Mobilities in The Fullerene Network of Conjugated Polymer-Based Solar Cells: Time-Resolved Microwave Conductivity and Theory. *Adv. Funct. Mater.* **2013**, *24*, 784−792.
(96) Clark, A. P.-Z.; Shi, C.; Ng, B. C.; Wilking, J. N.; Ayzner, A. L.; Stieg, A. Z.; Schwartz, B. J.; Mason, T. G.; Rubin, Y.; Tolbert, S. H. Self-Assembling Semiconducting Polymersâ Rods and Gels from Electronic Materials. *ACS Nano* **2013**, *7*, 962−977.
(97) Ayzner, A. L.; Tassone, C. J.; Tolbert, S. H.; Schwartz, B. J. Reappraising the Need for Bulk Heterojunctions in Polymer/Fullerene Photovoltaics: The Role of Carrier Transport in All-Solution-Processed P3HT/PCBM Bilayer Solar Cells. *J. Phys. Chem. C* **2009**, *113*, 20050−20060.
(98) Tremolet de Villers, B.; Tassone, C. J.; Tolbert, S. H.; Schwartz, B. J. Improving the Reproducibility of P3HT:PCBM Solar Cells by Controlling the PCBM/Cathode Interface. *J. Phys. Chem. C* **2009**, *113*, 18978−18982.
(99) Ayzner, A. L.; Doan, S. C.; Tremolet de Villers, B.; Schwartz, B. J. Ultrafast Studies of Exciton Migration and Polaron Formation in Sequentially Solution-Processed Conjugated Polymer/Fullerene Quasi-Bilayer Photovoltaics. *J. Phys. Chem. Lett.* **2012**, *3*, 2281−2287.
(100) Nardes, A. M.; Ayzner, A. L.; Hammond, S. R.; Ferguson, A. J.; Schwartz, B. J.; Kopidakis, N. Photoinduced Charge Carrier Generation and Decay in Sequentially Deposited Polymer/Fullerene Layers: Bulk Heterojunction vs Planar Interface. *J. Phys. Chem. C* **2012**, *116*, 7293−7305.
(101) Sawamura, M.; Kawai, K.; Matsuo, Y.; Kanie, K.; Kato, T.; Nakamura, E. Stacking of Conical Molecules with a Fullerene Apex into Polar Columns in Crystals and Liquid Crystals. *Nature* **2002**, *419*, 702−705.

(102) Marcus, R. A. Electron Transfer Reactions in Chemistry. Theory and Experiment. *Rev. Mod. Phys.* **1993**, *65*, 599−610.
(103) Dicker, G.; de Haas, M. P.; Siebbeles, L. D.; Warman, J. M. Electrodeless Time-Resolved Microwave Conductivity Study of Charge-Carrier Photogeneration in Regioregular Poly(3-Hexylthiophene) Thin Films. *Phys. Rev. B* **2004**, *70*, 045203.
(104) Ferguson, A. J.; Blackburn, J. L.; Holt, J. M.; Kopidakis, N.; Tenent, R. C.; Barnes, T. M.; Heben, M. J. Rumbles, G. Photoinduced Energy and Charge Transfer in P3HT:SWNT Composites. *J. Phys. Chem. Lett.* **2010**, *1*, 2406−2411.
(105) Hoven, C. V.; Garcia, A.; Bazan, G. C.; Nguyen, T.-Q. Recent Applications of Conjugated Polyelectrolytes in Optoelectronic Devices. *Adv. Mater.* **2008**, *20*, 3793−3810.
(106) Jiang, H.; Taranekar, P.; Reynolds, J. R.; Schanze, K. S. Conjugated Polyelectrolytes: Synthesis, Photophysics and Applications. *Angew. Chem.* **2009**, *48*, 4300−4316.
(107) Duarte, A.; Pu, K.-Y.; Liu, B.; Bazan, G. C. Recent Advances in Conjugated Polyelectrolytes for Emerging Applications. *Chem. Mater.* **2011**, *23*, 510−515.
(108) Liu, Y.; Ogawa, K.; Schanze, K. S. Conjugated Polyelectrolytes as Fluorescent Sensors. *J. Photochem. Photobiol. C* **2009**, *10*, 173−90.
(109) Thomas, S. W., III; Guy, D. J.; Swager, T. M. Chemical Sensors Based on Ampliying Fluorescent Conjugated Polymers. *Chem. Rev.* **2007**, *107*, 1339−1386.
(110) Tan, C.; Pinto, M. R.; Schanze, K. S. Photophysics, Aggregation and Amplified Quenching of a Water-Soluble Poly(Phenylene Ethynylene). *Chem. Commun.* **2002**, 446−447.
(111) Briseno, A. L.; Mannsfeld, S. C. B.; Shamberger, P. J.; Ohuchi, F. S.; Bao, Z.; Jenekhe, S. A.; Xia, Y. Self-Assembly, Molecular Packing, and Electron Transport in n-Type Polymer Semiconductor Nanobelts. *Chem. Mater.* **2008**, *20*, 4712−4719.
(112) Jiang, H.; Taranekar, P.; Reynolds, J.; Schanze, K. Conjugated Polyelectrolytes: Synthesis, Photophysics, and Applications. *Angew. Chem., Int. Ed.* **2009**, *48*, 4300−4316.
(113) Cadby, A. J.; Tolbert, S. H. Controlling Optical Properties and Interchain Interactions in Semiconducting Polymers by Encapsulation in Periodice Nanoporous Silicas with Different Pore Sizes. *J. Phys. Chem. B* **2005**, *109*, 17879−17886.
(114) Svergun, D. I.; Koch, M. H. J. Small-Angle Scattering Studies of Biological Macromolecules in Solution. *Rep. Prog. Phys.* **2003**, *66*, 1735−1782.
(115) Cassell, A. M.; Asplund, C. L.; Tour, J. M. Self-Assembling Supramolecular Nanostructures from a C_{60} Derivative: Nanorods and Vessicles. *Agnew. Chem.* **1999**, *38*, 2403−2405.
(116) Guldi, D. M.; Zerbetto, F.; Georgakilas, V.; Prato, M. Ordering Fullerenes at Nanometer Dimensions. *Acc. Chem. Res.* **2005**, *38*, 38−43.
(117) Yu, G.; Gao, J.; Hummelen, J. C.; Wudl, F.; Heeger, A. J. Polymer Photovoltaic Cells: Enhanced Efficiencies via a Network of Internal Donor-Acceptor Heterojunctions. *Science* **1995**, *270*, 1789−1791.
(118) Collins, B. A.; Li, Z.; Tumbleston, J. R.; Gann, E.; McNeill, C. R.; Ade, H. Absolute Measurement of Domain Composition and Nanoscale Size Distribution Explains Performance in PTB7:PC71BM Solar Cells. *Adv. Energy Mater.* **2013**, *3*, 65−74.
(119) Lee, K. H.; Schwenn, P. E.; Smith, A. R. G.; Cavaye, H.; Shaw, P. E.; James, M.; Krueger, K. B.; Gentle, I. R.; Meredith, P.; Burn, P. L. Morphology of All-Solution-Processed "Bilayer" Organic Solar Cells. *Adv. Mater.* **2011**, *23*, 766−770.
(120) Moon, J. S.; Takacs, C. J.; Sun, Y.; Heeger, A. J. Spontaneous Formation of Bulk Heterojunction Nanostructures: Multiple Routes to Equivalent Morphologies. *Nano Lett.* **2011**, *11*, 1036−1039.
(121) Daniel, H. M.; Krishnamoorthy, A.; Thummalakunta, L. N. S. A.; Haw, Y. C.; Joachim, L. Formation and Characterisation of Solution Processed Pseudo-Bilayer Organic Solar Cells. *Green* **2011**, *1*, 291−298.
(122) Gevaerts, V. S.; Koster, L. J. A.; Wienk, M. M.; Janssen, R. A. J. Discriminating between Bilayer and Bulk Heterojunction Polymer:-Fullerene Solar Cells Using the External Quantum Efficiency. *ACS Appl. Mater. Interfaces* **2011**, *3*, 3252−3255.
(123) Wang, D. H.; Moon, J. S.; Seifter, J.; Jo, J.; Park, J. H.; Park, O. O.; Heeger, A. J. Sequential Processing: Control of Nanomorphology in Bulk Heterojunction Solar Cells. *Nano Lett.* **2011**, *11*, 3163−3168.
(124) Zhu, R.; Kumar, A.; Yang, Y. Polarizing Organic Photovoltaics. *Adv. Mater.* **2011**, *23*, 4193−4198.
(125) Cho, S.-M.; Bae, J.-H.; Jang, E.; Kim, M.-H.; Lee, C.; Lee, S.-D. Solvent Effect of the Fibrillar Morphology on the Power Conversion Efficiency of a Polymer Photovoltaic Cell in a Diffusive Heterojunction. *Semicond. Sci. Technol.* **2012**, *27*, 125018.
(126) Li, H.; Wang, J. Layer-by-Layer Processed High-Performance Polymer Solar Cells. *Appl. Phys. Lett.* **2012**, *101*, 263901.
(127) Loiudice, A.; Rizzo, A.; Latini, G.; Nobile, C.; de Giorgi, M.; Gigli, G. Graded Vertical Phase Separation of Donor/Acceptor Species for Polymer Solar Cells. *Sol. Energy Mater. Sol. Cells* **2012**, *100*, 147−152.
(128) Loiudice, A.; Rizzo, A.; Biasiucci, M.; Gigli, G. Bulk Heterojunction versus Diffused Bilayer: The Role of Device Geometry in Solution p-Doped Polymer-Based Solar Cells. *J. Phys. Chem. Lett.* **2012**, *3*, 1908−1915.
(129) Vohra, V.; Arrighetti, G.; Barba, L.; Higashimine, K.; Porzio, W.; Murata, H. Enhanced Vertical Concentration Gradient in Rubbed P3HT:PCBM Graded Bilayer Solar Cells. *J. Phys. Chem. Lett.* **2012**, *3*, 1820−1823.
(130) Yang, H. Y.; Kang, N. S.; Hong, J.-M.; Song, Y.-W.; Kim, T. W.; Lim, J. A. Efficient Bilayer Heterojunction Polymer Solar Cells with Bumpy Donor-Acceptor Interface Formed by Facile Polymer Blend. *Org. Electron.* **2012**, *13*, 2688−2695.
(131) Lin, Y.; Ma, L.; Li, Y.; Liu, Y.; Zhu, D.; Zhan, X. Small-Molecule Solar Cells with Fill Factors up to 0.75 via a Layer-by-Layer Solution Process. *Adv. Energy Mater.* **2013**, *4*, 1300626.
(132) Schulze, K.; Uhrich, C.; Schüppel, R.; Leo, K.; Pfeiffer, M.; Brier, E.; Reinold, E.; Bäuerle, P. Efficient Vacuum-Deposited Organic Solar Cells Based on a New Low-Bandgap Oligothiophene and Fullerene C_{60}. *Adv. Mater.* **2006**, *18*, 2872−2875.
(133) Jin, H.; Tuomikoski, M.; Hiltunen, J.; Kopola, P.; Maaninen, A.; Pino, F. Polymer-Electrode Interfacial Effect on Photovoltaic Performances in Poly(3-Hexylthiophene):Phenyl-C61-butyric Acid Methyl Ester Based Solar Cells. *J. Phys. Chem. C* **2009**, *113*, 16807−16810.
(134) Nelson, J. Diffusion-Limited Recombination in Polymer-Fullerene Blends and its Influence on Photocurrent Collection. *Phys. Rev. B* **2003**, *67*, 155209.
(135) Finck, B. Y.; Schwartz, B. J. Understanding the Origin of the S-Curve in Conjugated Polymer/Fullerene Photovoltaics from Drift-Diffusion Simulations. *Appl. Phys. Lett.* **2013**, *103*, 053306.
(136) White, M. S.; Olson, D. C.; Shaheen, S. E.; Kopidakis, N.; Ginley, D. S. Inverted Bulk-Heterojunction Organic Photovoltaic Device Using a Solution-Derived ZnO Underlayer. *Appl. Phys. Lett.* **2006**, *89*, 143517.
(137) Gadisa, A.; Tumbleston, J. R.; Ko, D.-H.; Aryal, M.; Lopez, R.; Samulski, E. T. The Role of Solvent and Morphology on Miscibility of Methanofullerene and Poly(3-Hexylthiophene). *Thin Solid Films* **2012**, *520*, 5466−5471.
(138) Vohra, V.; Higashimine, K.; Murakami, T.; Murata, H. Addition of Regiorandom Poly(3-Hexylthiophene) to Solution Processed Poly(3-Hexylthiophene):[6,6]-Phenyl-C_{61}-Butyric Acid Methyl Ester Graded Bilayers To Tune The Vertical Concentration Gradient. *Appl. Phys. Lett.* **2012**, *101*, 173301.
(139) Kim, D. H.; Mei, J.; Ayzner, A. L.; Schmidt, K.; Giri, G.; Appleton, A. L.; Toney, M. F.; Bao, Z. Sequentially Solution-Processed, Nanostructured Polymer Photovoltaics Using Selective Solvents. *Energy Environ. Sci.* **2014**, *7*, 1103−1109.
(140) Brabec, C. J.; Zerza, G.; Cerullo, G.; De Silvestri, S.; Luzzati, S.; Hummelen, J. C.; Sariciftci, S. Tracing Photoinduced Electron Transfer Process in Conjugated Polymer/Fullerene Bulk Heterojunctions in Real Time. *Chem. Phys. Lett.* **2001**, *340*, 232−236.